JOURNAL OF COMPUTATIONAL PHYSICS **123,** 415–434 (1996)
ARTICLE NO. 0034

Linear Instability Analysis for Toroidal Plasma Flow Equilibria

V. VARADARAJAN AND G. H. MILEY

University of Illinois at Urbana-Champaign, Urbana, Illinois 61801

Received May 3, 1993; revised November 30, 1994

The non-self-adjoint Frieman–Rotenberg equation for the linear ideal magnetohydrodynamic modes in flow equilibria is numerically solved in shaped finite-aspect ratio axisymmetric tokamak geometry. A quadratic form is derived from this equation, and, in particular, the self-adjoint force operator with finite toroidal rotation is cast into a manifestly self-adjoint form. The toroidal rotational velocities in the subsonic regime are considered. The quadratic form is discretized by a mixed finite-element procedure in the radial direction and by Fourier modes in the periodic directions. The mode frequency of the unstable mode is located by root searching, and the final root refinement is obtained by a rapid inverse iteration procedure for complex roots. The real part of the $n = 1$ internal kink mode scales linearly with the plasma rotation, and the imaginary part of the unstable mode is at least an order of magnitude higher in the presence of high plasma rotation velocities. The kink mode is also found to be unstable at high rotation velocities, even when the axis safety factor is above unity. The instability characterized by these features is termed here as the "centrifugal" instability. The centrifugal kink instability would have finite real parts, as shown by the plasma rotation observed in plasma devices such as tokamaks. To explain the features of this mode, the plasma rotation should be taken into account. Therein lies the usefulness of the computational analysis presented here.

INTRODUCTION

The problem of the stability of flowing plasmas has attracted considerable attention recently, especially in laboratory plasma physics. The analysis of Kelvin–Helmholtz instabilities, using a primitive variable formulation, is well established in space physics and astrophysics. The stability of the static tokamak plasma equilibria has been understood well since the work of Bernstein *et al.* [1]. However, our understanding of the MHD (magnetohydrodynamic) stability of the rotating tokamak plasma equilibria is rather incomplete, because the linear instability equations for the rotating plasma are not self-adjoint and the powerful tools available for the self-adjoint equations cannot be utilized to derive analytical results.

In fact, the laboratory plasmas found in tokamaks often experience significant toroidal velocities, especially during neutral beam injection [2]. The flows involved are dominantly toroidal and typically lie in the low end of the subsonic regime. Several new kinds of plasma instabilities can be destabilized at high flow velocities. For example, the eigenfrequencies of the rotating plasma kink modes have been experimentally observed and can be computationally verified. Despite this, many existing numerical equilibrium and stability codes employ full geometric features but still do not consider plasma rotation. As a result, various linear instability estimates used in the internal and external kink calculations are approximate.

The situation with respect to the study of rotating plasma instabilities is changing, albeit slowly. Several linear rotational instability calculations have been published recently in the astrophysical literature, as well as in the tokamak literature. Also, some results for the local stability of the rotating plasmas have been derived [3–4]. An analytical study of the ideal MHD, CGL, and Grad's GCP [5] equilibria with flows has been performed using a large aspect-ratio approximation. These results pertain mainly to high speed regimes. Also, considerable work has been done on the Kelvin–Helmholtz (KH) instability for specific equilibrium configurations. This instability is intensified at Alfven velocities. The KH instability of velocity shear layers has been investigated to study the interaction of the solar wind with the planet magnetospheres [6–8].

Another class of astrophysical phenomena that involves plasma flows, and for which the knowledge of instability properties is desired, involves collimated jets. The stability of different cylindrical configurations, both in azimuthal and longitudinal fields, has been investigated. But these analyses assume a step function in the equilibrium profile, either in the magnetic field or in the velocity profile. The effect of increasingly smooth velocity profiles in the case of planar flow has been investigated recently [9], and the importance of smooth profiles for revealing the realistic characteristics of the instability has been greatly emphasized. The KH instability has been analyzed for equilibria with the velocity parallel to the magnetic field in the case of rigidly rotating plasma and in the case of helical flow [10–11]. In addition, a helical configuration with an axial flow has been investigated for a single wave number [5]. A model of extragalactic jet equilibrium with continuous profiles has been investigated for instability in cylindrical geometry [12–14]. A summary of research on extragalactic jet instabilities is also available [14]. The stability of differ-

0021-9991/96 $18.00

ent cylindrical configurations in the presence of confining magnetic field and longitudinal flow has been investigated in the context of astrophysical applications [15–17]. The effect of flows on the resistive tearing modes has been investigated as well, but the problem does not represent ideal MHD.

The problem of rotating plasma equilibria in magnetic confinement fusion has attracted increasing attention in recent years, owing to the significant toroidal plasma velocity induced by beam injection into a tenuous plasma prevailing in the experimental tokamaks. Nevertheless, the influence of rotation on kink modes, as well as the microinstability modes in the magnetic confinement devices, has never been precisely estimated. Thus we have undertaken a computational study of the rotating internal kinks in realistic toroidal geometries.

In this paper, internal kinks in the presence of toroidal flow in axisymmetric tokamak geometry are analyzed using a Lagrangian perturbation formalism, first developed by Frieman and Rotenberg [18] for scalar pressure equilibria. A suite of codes has been developed to calculate flow equilibria and their instability characteristics. The equilibrium is solved using the FLOE (flow equilibrium) code in a generalized polar coordinate system using a multigrid method. Subsequently the results are mapped onto a flux coordinate system. The equilibrium results are written out to serve as input to the instability analysis. In the PINK (plasma internal kink) code used for the instability analysis, the perturbation amplitudes are written in a tensor product formalism, using Fourier modes in the periodic direction and mixed finite-elements in the radial direction. The resulting set of equations is solved numerically for the eigenfrequency and eigenvector of the most unstable internal kink mode. The eigenfrequency is approximately located in the complex plane by a visual search of the determinant data. Then the eigenfrequency is refined by inverse iteration and is verified by solving a quadratic equation.

LAGRANGIAN PERTURBATION EQUATIONS

The perturbation equations are derived via a Lagrangian formalism. The discretized numerical eigenvalue problem resulting from this formalism is compact, since only three vectors need to be discretized, reducing the dimension of the discretized system.

A Lagrangian perturbation theory for analyzing the stationary states of the stars has long been the subject of interest in astrophysics and geophysics [19–21]. However, this procedure has not been widely used to study the kink stability of the axisymmetric rotating plasma equilibria. Nevertheless, certain approximate estimates of the pinch plasma instability [22] have been derived using circle theorems, and some large aspect-ratio analyses have been performed. Also, the instability equations for stationary plasma equilibria have been derived [23] using the critical point properties of the Lyapunov functional for one fluid nondissipative MHD.

The Frieman–Rotenberg-type perturbed Lagrangian equation is derived in the following using an axiomatic approach. This approach is thought to be more transparent than the original derivation by Frieman and Rotenberg [18].

The perturbed flow is described by specifying, at each instant, the displacement $\boldsymbol{\xi}(\mathbf{x}, t)$ which an element of the fluid in the perturbed flow experiences relative to its dynamic location in the unperturbed flow $\mathbf{x}(t)$. The displacement $\boldsymbol{\xi}(x, t)$ is assumed to be small and only first-order perturbations in the MHD equation are retained. Details of the procedures outlined here can also be found in the literature [18–19, 24–28]. Now consider the value of an attribute Q of a perturbed fluid element located at $\mathbf{x} + \boldsymbol{\xi}(\mathbf{x}, t)$ at time t. The Lagrangian change caused by the perturbaton in Q is formally denoted by ΔQ:

$$\Delta Q = Q(\mathbf{x} + \boldsymbol{\xi}(\mathbf{x}, t), t) \cong Q_0(\mathbf{x}, t). \tag{1}$$

The change in Q perceived by an observer at the same location $x(t)$ in the stationary flow is an Eulerian change and is denoted by δQ:

$$\delta Q = Q(\mathbf{x}, t) - Q_0(\mathbf{x}, t). \tag{2}$$

By Taylor expanding $Q(\mathbf{x} + \boldsymbol{\xi}, t)$ to first order, we find that

$$\Delta Q = \delta Q + \xi j \frac{\partial Q}{\partial x_j}. \tag{3}$$

Since this relation is valid for any scalar attribute, the following equality is obtained when the operator is applied to scalar variables:

$$\Delta = \delta + \xi_j \frac{\partial}{\partial x_j} = \delta + \boldsymbol{\xi} \cdot \nabla. \tag{4}$$

The Lagrangian change in fluid velocity is given by

$$\Delta \mathbf{v} = \frac{d\boldsymbol{\xi}}{dt}, \tag{5}$$

while the observation of mass of a Lagrangian element of the perturbed flow is given by

$$\Delta \rho = -\rho \nabla \cdot \boldsymbol{\xi}. \tag{6}$$

The corresponding Eulerian perturbations are useful in the derivation of the perturbation equation. Thus,

$$\delta\rho = -\nabla\cdot(\rho\boldsymbol{\xi}), \tag{7}$$

$$\delta\mathbf{v} = \frac{\partial\boldsymbol{\xi}}{\partial t} + \mathbf{v}\cdot\nabla\boldsymbol{\xi} - \boldsymbol{\xi}\cdot\nabla\mathbf{v}. \tag{8}$$

The Lagrangian perturbation of the magnetic field is derived using a subtle property of the magnetic field in ideal MHD [29]. Two conditions for the ideal MHD, namely,

$$\mathbf{E} + \mathbf{v}\times\mathbf{B} = 0, \tag{9}$$

$$\nabla\times\mathbf{E} = -\frac{\partial\mathbf{B}}{\partial t}, \tag{10}$$

lead to

$$\frac{\partial\mathbf{B}}{\partial t} = \nabla\times(\mathbf{v}\times\mathbf{B}). \tag{11}$$

From this and the continuity equation, it can be shown that

$$\frac{d}{dt}\left(\frac{\mathbf{B}}{\rho}\right) = \frac{\mathbf{B}}{\rho}\cdot\nabla\mathbf{v}. \tag{12}$$

This formula can be interpreted as follows. The relative distance between two points can vary as

$$\frac{d}{dt}(\mathbf{x}_2 - \mathbf{x}_1) = (\mathbf{x}_2 - \mathbf{x}_1)\cdot\nabla\mathbf{v}, \tag{13}$$

and relative changes in $\mathbf{B}/\rho$ obey the same type of variation as in Eq. (13). If two points are on the same field line and lie close together, after an infinitesimal change in time, they still lie on the same field line, while the vector $\mathbf{B}/\rho$ varies proportionately to their distance. Since the mass of the fluid is conserved, volume changes must obey the relation

$$\rho(\mathbf{x}+\boldsymbol{\xi})J(\mathbf{x}+\boldsymbol{\xi},\mathbf{x}) = \rho(\mathbf{x}). \tag{14}$$

Note that the Jacobian of this volume change is

$$J(\mathbf{x}+\boldsymbol{\xi},\mathbf{x}) = 1 + \nabla\cdot\boldsymbol{\xi}. \tag{15}$$

By integrating Eq. (13) to obtain the variation of $\mathbf{B}/\rho$ in the Lagrangian frame, and noting that $v = d\boldsymbol{\xi}/dt$ represents the Lagrangian velocity between the perturbed and unperturbed flow, we obtain

$$\frac{\mathbf{B}(\mathbf{x}+\boldsymbol{\xi})}{\rho(\mathbf{x}+\boldsymbol{\xi})} - \frac{\mathbf{B}(\mathbf{x})}{\rho(\mathbf{x})} = \int\frac{\mathbf{B}(\mathbf{x})}{\rho(\mathbf{x})}\cdot\nabla\left[dt\,\frac{d\boldsymbol{\xi}}{dt}\right]. \tag{16}$$

Hence,

$$\mathbf{B}(\mathbf{x}+\boldsymbol{\xi}) = \mathbf{B}(\mathbf{x}) - \mathbf{B}\,\nabla\cdot\boldsymbol{\xi} + \mathbf{B}\cdot\nabla\boldsymbol{\xi}, \tag{17}$$

to first order in $\boldsymbol{\xi}$.

The perturbed Lagrangian momentum equation is derived by applying the Δ operator to the momentum equation divided by the density ρ and multiplying the result by ρ. The resulting equation is

$$\rho\,\Delta\left\{\frac{d\mathbf{v}}{dt} = -\frac{1}{\rho}\nabla p + \frac{1}{\rho}[\nabla\times\mathbf{B}]\times\mathbf{B}\right\}. \tag{18}$$

Since Δ and d/dt commute to first order in $\boldsymbol{\xi}$, the substantial derivative in Eq. (18) transforms as

$$\begin{aligned}\rho\frac{d\,\Delta\mathbf{v}}{dt} &= \rho\frac{d}{dt}\frac{d\boldsymbol{\xi}}{dt} = \rho\frac{d}{dt}(\boldsymbol{\xi}_t + \mathbf{v}\cdot\nabla\boldsymbol{\xi})\\ &= \rho(\boldsymbol{\xi}_{tt} + 2\mathbf{v}\cdot\nabla\boldsymbol{\xi}_t + (\mathbf{v}\cdot\nabla)^2\boldsymbol{\xi}).\end{aligned} \tag{19}$$

The Lagrangian perturbations of the pressure and the $\mathbf{J}\times\mathbf{B}$ terms are derived using the identity (4) connecting Δ and δ. The resulting form is

$$\begin{aligned}\Delta\left[\frac{1}{\rho}(-\nabla p + (\nabla\times\mathbf{B})\times\mathbf{B})\right] &= \delta\left[\frac{1}{\rho}(-\nabla p + (\nabla\times\mathbf{B})\times\mathbf{B})\right]\\ &\quad + \boldsymbol{\xi}\cdot\nabla\left[\frac{1}{\rho}(-\nabla p + (\nabla\times\mathbf{B})\times\mathbf{B})\right].\end{aligned} \tag{20}$$

An intermediate form of the perturbed momentum equation can be found by combining Eqs. (19)–(20). It is written as

$$\begin{aligned}&\rho\left[\frac{\partial^2\boldsymbol{\xi}}{\partial t^2} + 2\rho\mathbf{v}\cdot\nabla\boldsymbol{\xi}_t + \rho(\mathbf{v}\cdot\nabla)^2\boldsymbol{\xi}\right]\\ &\quad = +\frac{\Delta\rho}{\rho}\nabla p + \frac{1}{\rho}\delta(\nabla p) - \frac{1}{\rho}\boldsymbol{\xi}\cdot\nabla(\nabla p) - \frac{\Delta\rho}{\rho}(\nabla\times\mathbf{B})\times\mathbf{B}\\ &\qquad + \frac{1}{\rho}[(\nabla\times\delta\mathbf{B})\times\mathbf{B} + (\nabla\times\mathbf{B})\times\delta\mathbf{B}]\\ &\qquad + \frac{1}{\rho}\boldsymbol{\xi}\cdot\nabla[(\nabla\times\mathbf{B})\times\mathbf{B}].\end{aligned} \tag{21}$$

After substituting for $\Delta\rho$ from Eq. (6), rearranging the terms, and using the MHD equilibrium equation and the continuity equation $\nabla\cdot(\rho\mathbf{v}) = 0$, we can reduce the

perturbation equation for scalar pressure equilibrium to

$$\rho\boldsymbol{\xi}_{tt} + 2\rho\mathbf{v}\cdot\nabla\boldsymbol{\xi}_t = -\nabla\delta p + [(\nabla\times\delta\mathbf{B})\times\mathbf{B} + (\nabla\times\mathbf{B})\times\delta\mathbf{B}] + \nabla\cdot[\boldsymbol{\xi}(\rho\mathbf{v}\cdot\nabla\mathbf{v}) - \rho\mathbf{v}(\mathbf{v}\cdot\nabla\boldsymbol{\xi})], \quad (22)$$

where $\mathbf{v}$ and $\mathbf{B}$ are, respectively, the equilibrium velocity profile and the magnetic field profile.

The first term on the right-hand side in Eq. (22) is rewritten as follows. We assume an adiabatic equation state applies. Then, the density and pressure perturbations can be related as

$$\frac{\Delta p}{p} = \gamma\frac{\Delta\rho}{\rho}, \quad (23)$$

giving

$$\Delta p = -\gamma p\,\nabla\cdot\boldsymbol{\xi}, \quad (24)$$

$$\delta p = -\gamma p\,\nabla\cdot\boldsymbol{\xi} - \boldsymbol{\xi}\cdot\nabla p. \quad (25)$$

In the following sections γ is set to $\frac{5}{3}$, representing an adiabatic equation of state for the plasma. The perturbations in the Eulerian coordinates are related to the components of $\boldsymbol{\xi}$ through

$$\mathbf{B}_1 = \delta\mathbf{B} = \mathbf{Q} = \Delta\mathbf{B} - \boldsymbol{\xi}\cdot\nabla\mathbf{B}$$

$$= \mathbf{B}(\mathbf{x}+\boldsymbol{\xi}) - \mathbf{B}(\mathbf{x}) - \boldsymbol{\xi}\cdot\nabla\mathbf{B} \quad (26)$$

$$= \nabla\times(\boldsymbol{\xi}\times\mathbf{B}), \quad (27)$$

$$\rho_1 = \delta\rho = -\nabla\cdot(\rho\boldsymbol{\xi}), \quad (28)$$

$$\mathbf{v}_1 = \delta\mathbf{v} = \boldsymbol{\xi}_t + \mathbf{v}\cdot\nabla\boldsymbol{\xi} - \boldsymbol{\xi}\cdot\nabla\mathbf{v}. \quad (29)$$

These perturbations are useful when the calculations are compared to the experimental data in the lab coordinate system.

For the normal modes with time dependence as $\exp(-i\omega t)$, Eq. (22) can be written as

$$-\rho\omega^2\boldsymbol{\xi} - 2i\omega\rho\mathbf{v}\cdot\nabla\boldsymbol{\xi} = \mathbf{F}(\boldsymbol{\xi}) = -\nabla\delta p + [(\nabla\times\mathbf{Q})\times\mathbf{B} + (\nabla\times\mathbf{B})\times\mathbf{Q}] + \nabla\cdot[\boldsymbol{\xi}(\rho\mathbf{v}\cdot\nabla\mathbf{v}) - \rho\mathbf{v}(\mathbf{v}\cdot\nabla\boldsymbol{\xi})]. \quad (30)$$

The computational solution of Eq. (30) forms the core of this paper. A number of the formal properties of the operators in Eq. (30) can be summarized as follows: (a) $i\rho\mathbf{v}\cdot\nabla$ is a Hermitian operator; (b) $\mathbf{F}(\boldsymbol{\xi}) = -\nabla\delta p + [(\nabla\times\mathbf{Q})\times\mathbf{B} + (\nabla\times\mathbf{B})\times\mathbf{Q}] + \nabla\cdot[\boldsymbol{\xi}(\rho\mathbf{v}\cdot\nabla\mathbf{v}) - \rho\mathbf{v}(\mathbf{v}\cdot\nabla\boldsymbol{\xi})]$ is a self-adjoint operator for scalar pressure one-fluid stationary MHD equilibrium; (c) if $\omega = \alpha$ is an eigenvalue, $\omega = -\alpha$, $\omega = \alpha^*$, $\omega = -\alpha^*$ are also eigenvalues.

Equation (30) is not self-adjoint. Thus a direct establishment of an energy principle is not possible. However, the problem is computationally tractable if a bilinear form is derived. For this, Eq. (30) is multiplied by $\boldsymbol{\xi}^*$ and integrated by parts, to make the force operator $\mathbf{F}(\boldsymbol{\xi})$ manifestly self-adjoint. The resulting bilinear form reduces to the standard energy principle in the limit of vanishing velocities. The self-adjoint form in scalar pressure equilibria appears to differ from that published for the case of a rotating plasma with anisotropic pressure [32]. However, one cannot directly compare the two different forms, since the CGL equation of state assumed in [32] does not reduce to the adiabatic equation of state used here in the limiting case of isotropic pressure and creates the irreconcilable differences. Also, another bilinear form of Eq. (22) has been given in the context of ballooning stability analysis [33].

To write the results in a form closely resembling the quadratic form of Bernstein *et al.* [1], which still readily reduces to a PEST code formulation, we employ familiar partial integration procedures to obtain a new quadratic form. The details of the derivation are given in Ref. [34]. The resulting quadratic form for the normal modes and with finite toroidal rotation is

$$\omega^2\int d^3\mathbf{x}\times\rho\boldsymbol{\xi}^*\cdot\boldsymbol{\xi} + 2i\omega\int d^3\mathbf{x}\times\boldsymbol{\xi}^*\cdot(\rho\mathbf{v}\cdot\nabla\boldsymbol{\xi})$$

$$= \int d^3\mathbf{x}\times\left\{\gamma p|\nabla\cdot\boldsymbol{\xi}|^2 + \left|\mathbf{Q} + \frac{\boldsymbol{\xi}\cdot\nabla\psi}{|\nabla\psi|^2}\mathbf{J}\times\nabla\psi\right|^2 - 2\,\nabla\psi\cdot\boldsymbol{\kappa}\frac{|\boldsymbol{\xi}\cdot\nabla\psi|^2}{|\nabla\psi|^2}\frac{\nabla\psi\cdot\nabla p}{|\nabla\psi|^2} + S\frac{\mathbf{B}\cdot\mathbf{J}}{B^2}|\boldsymbol{\xi}\cdot\nabla\psi|^2 - \frac{|\boldsymbol{\xi}\cdot\nabla\psi|^2}{|\nabla\psi|^2}\left(\frac{\mathbf{J}\cdot\mathbf{B}}{B}\right)^2 - 2\,\nabla\psi\cdot\boldsymbol{\kappa}\frac{|\boldsymbol{\xi}\cdot\nabla\psi|^2}{|\nabla\psi|^2}\frac{\nabla\psi\cdot(\rho\mathbf{v}\cdot\nabla\mathbf{v})}{|\nabla\psi|^2} - \boldsymbol{\xi}\cdot(\rho\mathbf{v}\cdot\nabla\mathbf{v})\,\nabla\cdot\boldsymbol{\xi}^* - \boldsymbol{\xi}^*\cdot(\rho\mathbf{v}\cdot\nabla\mathbf{v})\,\nabla\cdot\boldsymbol{\xi} - \rho|\mathbf{v}\cdot\nabla\boldsymbol{\xi}|^2 + \boldsymbol{\xi}^*\cdot(\boldsymbol{\xi}\cdot\nabla)\,\nabla p - \boldsymbol{\xi}^*\cdot\nabla\psi\,\boldsymbol{\xi}\cdot\nabla\left(\frac{\nabla\psi\cdot\mathbf{J}\times\mathbf{B}}{|\nabla\psi|^2}\right) - \boldsymbol{\xi}\cdot\nabla\psi\,\boldsymbol{\xi}^*\cdot\nabla\left(\frac{\nabla\psi\cdot\mathbf{J}\times\mathbf{B}}{|\nabla\psi|^2}\right) - \boldsymbol{\xi}^*\cdot(\boldsymbol{\xi}\cdot\nabla)\,\nabla\psi\frac{\nabla\psi\cdot\mathbf{J}\times\mathbf{B}}{|\nabla\psi|^2} + \frac{|\boldsymbol{\xi}\cdot\nabla\psi|^2}{|\nabla\psi|^2}\nabla\psi\cdot\nabla\left(\frac{\nabla\psi\cdot\mathbf{J}\times\mathbf{B}}{|\nabla\psi|^2}\right)\right\}. \quad (31)$$

The computational forms of various terms in Eq. (31) are outlined in Appendix A. Here, the term S is the local shear and is defined in Appendix A. All the terms on the right-hand side of Eq. (31) are manifestly self-adjoint. Equation (31) reduces to the self-adjoint form of the potential energy popularly used in the PEST [35], ERATO [30–31], and

KERNER [36] codes in the limit of vanishing equilibrium velocity.

Only internal kinks are studied here. Since the normal component of $\boldsymbol{\xi}$ vanishes on the plasma surface, the boundary terms arising from the integration by parts vanish.

NUMERICAL ANALYSIS OF LINEAR INSTABILITY PROBLEM

The problem posed by Eq. (31) can only be solved numerically, because of the complexity of the equations and because of the desire to obtain results for practical tokamak configurations. The nature of the numerical analysis employed, the methodology adopted, several benchmark comparisons carried out, and some new results obtained are given in this section.

When the differential equations are simpler, resembling the equations of continuum mechanics and simple partial differential equations, several standard techniques can be used for eigensystem and evolution problems [37–39]. However, the MHD equations pose a unique set of problems. Several earlier studies into the nature of the problem have resulted in robust codes [30, 35, 36, 40]. The eigenvalue problem in the ideal MHD approximation is summarized in Ref. [31]. Therein only the static MHD problem is considered, but here we employ some of the ideas for the rotating MHD stability problem. In the following the tensor product expansion of displacement $\boldsymbol{\xi}$ is the starting point, leading to a discretization of the problem.

The perturbed components are expanded following a standard practice adopted in the ERATO code [30–31]. The perturbation vector $\boldsymbol{\xi}$ is written as

$$\boldsymbol{\xi} = XR^2\,\nabla\theta \times \nabla\phi + VR^2\,\nabla\theta \times \nabla\phi + ZR^2\mathbf{B}. \quad (32)$$

Here X, V, and Z are, respectively, the scalar amplitudes of $\boldsymbol{\xi}$ along the contravariant directions $\nabla\theta \times \nabla\phi$ and $\nabla\theta \times \nabla\phi$ and the mixed-tensor direction $\mathbf{B}$. Then, with $\mathbf{B} = \nabla\phi \times \nabla\psi + J\nabla\phi$, the magnetic field perturbation vector $\mathbf{Q}$ can be written as

$$\begin{aligned}\mathbf{Q} \equiv \nabla \times (\boldsymbol{\xi} \times \mathbf{B}) = {} & \nabla\psi \times \nabla\theta\,[-(VJ)_\theta - (XJ)_\phi] \\ & + \nabla\theta \times \nabla\phi\,[(XJ)_\phi + (XR^2/J)_\theta] \\ & + \nabla\phi \times \nabla\psi\,[(VJ)_\phi - (XR^2/J)_\psi].\end{aligned} \quad (33)$$

In our study, the perturbations X, V, and Z are expressed using Fourier modes in the theta direction and mixed finite elements in the radial direction. The kink mode eigenfunctions are usually computed using finite elements in the radial direction. The mixed finite element formulation is used in order to compute eigenvalues correctly, avoiding numerical "pollution." The mixed finite element approximation used here is yet to be rigorously proven to be pollution free, but our computational experiments show that it yields an unstable eigenvalue spectrum similar to a pollution-free static MHD spectrum, even for large toroidal rotation velocities. However, both the stable and unstable sides of the eigenvalue spectrum have yet to be computed with finite rotation to study the convergence properties of the discretization in detail.

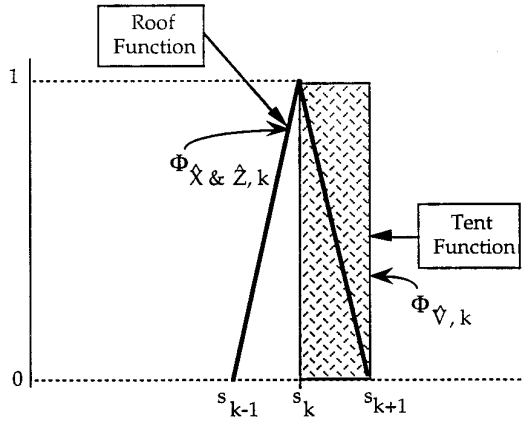

FIG. 1. Mixed-finite element representation used for the discretization of radial components of the eigenfunctions.

The finite element roof (1D triangular element) and tent (1D step element) functions are used in the radial direction. These are the lowest-order finite elements that can be employed in our problem. A new flux function "s" and new scalar perturbation components $\hat{X}$, $\hat{V}$, and $\hat{Z}$ are introduced as

$$s = \sqrt{\psi/\psi_0}, \quad (34)$$

$$\hat{X} = X, \quad (35a)$$

$$\hat{V} = 2s\psi_0 V, \quad (35b)$$

$$\hat{Z} = 2s\psi_0 Z. \quad (35c)$$

The radial functions of $\hat{X}$ and $\hat{Z}$ are discretized by the roof functions, and the radial function of $\hat{V}$ is discretized by the tent function. The finite element shape functions are shown in Fig. 1 These functions are defined in a generic interval in s over the nodes $[k-1, k, k+1]$ as

$$\Phi_{\text{roof}} = \left\{ \Phi_k | \Phi_k = \frac{s - s_{k+1}}{s_k - s_{k+1}} \qquad \forall s \in [s_k, s_{k+1}]; \right.$$

$$\left. \Phi_k = \frac{s - s_{k-1}}{s_k - s_{k-1}} \qquad \forall s \in [s_{k-1}, s_k];\ \Phi_k = 0 \text{ elsewhere} \right\};$$

$$\Phi_{\text{tent}} = \{\Phi_k | \Phi_k = 1\ \forall s \in [s_k, s_{k+1}];\ \Phi_k = 0 \text{ elsewhere}\}.$$

For instability analysis, the equilibrium results are mapped onto a nonuniform mesh in the radial direction. The nonuniform mesh is necessary to increase the number of nodes where the eigenfunctions have steep changes, especially near the critical surfaces. Thus, the perturbations $\hat{X}$, $\hat{V}$, $\hat{Z}$ are expressed in the familiar tensor product form as

$$\xi = \sum_{1}^{K} \sum_{-M/2}^{M/2} \hat{\xi}_{kmn} \Phi_k(s) \exp[i(m\theta - n\phi - \omega t], \qquad (36)$$

where $\Phi_k(s)$ is the kth finite element in variable $s \in [0, 1]$, there are K radial nodes, $\hat{\xi}_{kmn}$ are the amplitudes of the corresponding modes, and $M + 1$ is the total number of poloidal modes for each perturbed variable, where M is an even number. In particular, $\hat{\xi}_{kmn}$ stands for the kth finite element amplitude of a mode with poloidal model number m and toroidal mode number n. The regularity conditions at the magnetic axis are $\hat{X} = \hat{V} = \hat{Z} = 0$, and the boundary condition at the outer flux surface is $\hat{X} = 0$. There are $(3K - 4)(M + 1)$ mode amplitudes. Thus $(3K - 4)(M + 1)$ equations are required to completely specify the problem. The quadratic form is discretized by completing the θ and radial integrations. The resulting computational form is

$$\langle \hat{\xi}^*_{kmn} | - \omega^2 A - 2i\omega C + B | \hat{\xi}_{lm'n} \rangle = 0. \qquad (37)$$

Typically, we restrict the study to the case of the $n = 1$ mode. The variation of this bilinear form with respect to $\hat{\xi}^*_{kmn}$ yields a set of simultaneous equations for the $\hat{\xi}_{kmn}$. The boundary conditions are imposed on this set of equations. The vector X, consisting of amplitudes of $\hat{\xi}_{kmn}$, is obtained after varying (37) with respect to $\boldsymbol{\xi}^*$ as

$$-\omega^2 AX - i\omega CX + BX = 0, \qquad (38)$$

where X represents the complex vector consisting of all the discrete amplitudes $\hat{\xi}_{kmn}$ for all k, m and one fixed n. This set of equations is analogous to the Raleigh problem for the frequency ω and the eigenvector X. The eigenfrequencies are the roots of

$$\det |-\omega^2 A - i\omega C + B| = 0. \qquad (39)$$

The matrices A, B, and C are calculated and stored in row-shifted band matrix form. The matrices A and B are Hermitian, and C is anti-Hermitian. The calculations are done using MKSA units. To minimize numerical corruption, the multiplier $\sqrt{\rho\mu_0}$ is factored out, so the modified eigenfrequency is given by $\omega\sqrt{\rho\mu_0}$. The radial integrals are obtained by a two-point Gaussian integration.

The eigenfrequency and the eigenvector of the most unstable kink mode are determined by a two-step iterative process. First, the roots are approximately located in the complex plane by investigating the sign of the determinant in Eq. (39) for various values of ω. For a given value of ω, the determinant is calculated by utilizing the IMSL library routines LFCCB and LFDCB. The routine LFCCB performs a LU decomposition with pivoting, and the routine LFDCB calculates the determinant as the product of the diagonal elements in the upper triangular component. Then an inverse iteration procedure is used to refine the root once an approximate root ω_a is determined. To start the inverse iteration procedure, an approximate eigenvector is specified, first using smooth perturbation profiles, and then superimposing a random vector. In the inverse iteration process, the vector–band–matrix multiplications are done using the IMSL routine CGBMV, LU factorization is carried out with the IMSL routine LFCCB, and linear systems are solved using the IMSL routine LFSCB. For a specified approximate root ω_a, the root refinement problem is formulated as an eigenvalue problem with root shifting. The root and eigenvector refinement employs inverse iteration, and it can be explained as follows.

Let the approximate root ω_a remain the same throughout and let ω_c be the correction, so that the desired root is $\omega = \omega_a + \omega_c$. Let the eigenvector at stage k for $k \geq 0$ in inverse iteration be X_k. X_k is normalized to unit amplitude. Then the eigenvector at stage $k + 1$ and the root correction ω_c obey the equation

$$\begin{aligned}(B - \omega_s^2 A - i(\omega_a + \omega_c)C)X_{k+1} &= \omega_c(\omega_c + 2\omega_a)AX_k \\ &= \lambda_{k+1} 2\omega_a AX_k, \qquad (40a)\end{aligned}$$

$$(B - \omega_s^2 A - i(\omega_a + \omega_c)C)Y_{k+1} = 2\omega_a AX_k, \qquad (40b)$$

where

$$Y_{k+1} = X_{k+1}/\lambda_{k+1}. \qquad (40c)$$

Equations (40a)–(40c) constitute the inverse iteration procedure [39, 41] for the complex eigenvalue $\omega = \omega_a + \omega_c$. Since the correction ω_c and, hence, the eigenvalue λ_{k+1} in Eq. (40a) are small, the inverse iteration process can be shown to converge rapidly to the eigenvector and yield the correction factor λ_{k+1} as well. The inverse iteration can be thought of as a series of linear system solutions around the new and small eigenvalue of λ_{k+1}. Further details of this process are as follows. For a given unit vector X_k, vector Y_{k+1} is solved for, and λ_{k+1} is obtained as follows. The absolute value of λ_{k+1} is given by

$$\|\lambda_{k+1}\| = 1/\|Y_{k+1}\|, \qquad (41)$$

and the complex phase factor in λ_{k+1} is obtained as

$$\lambda_{k+1}/\|\lambda_{k+1}\| = X_k/[\|\lambda_{k+1}\|Y_{k+1}], \quad (42)$$

where the division is done term by term in Eq. (42) and averaged; i.e.,

$$(\lambda_{k+1}/\|\lambda_{k+1}\|)_{,i} = X_{k,i}/[\|\lambda_{k+1}\|Y_{k+1,i}]. \quad (43)$$

The subscript i in Eq. (43) represents the ith value of the new phase factor obtained from the ith amplitudes of X_k and Y_{k+1}. These phase factors are summed and averaged to obtain λ_{k+1} as

$$\lambda_{k+1} = \|\lambda_{k+1}\| \times (\text{average phase factor}). \quad (44)$$

This value of λ_{k+1} is used to solve the quadratic equation

$$\omega_c(\omega_c/2\omega_a + 1) = \lambda_{k+1}, \quad (45)$$

and ω_c is obtained as a small correction to ω_a. The correction value ω_c is substituted in Eq. (40a) at regular intervals, but not in every iteration $k + 1$, so that only the converged ω_c is substituted on the left-hand side. This substitution procedure further guarantees convergence.

For increasing values of toroidal rotation velocities, the values of ω_a and ω_c are found by continuation, increasing Ω in small steps. The roots are accepted only when the results from the inverse iteration procedure and a direct solution for ω using the eigenvector given by the inverse iteration procedure agree. This direct solution for ω can be obtained by considering the bilinear form as a quadratic equation for ω: thus the direct solution of ω is given as

$$\omega = [iX^{\dagger}CX \pm \sqrt{-(X^{\dagger}CX)^2 + 4X\dagger AX(X^{\dagger}BX)}/[2X^{\dagger}AX], \quad (46)$$

where X is the eigenvector obtained from the inverse iteration procedure, and $X^{\dagger}$ is its conjugate transpose. This direct solution of ω should be equal to the sum of the approximate root ω_a and a correction ω_c, as calculated earlier.

By visually locating the root by scanning for the zeros of the determinant Eq. (39), then improving the root by inverse iteration, and subsequently using the root validation procedure given above, we can finalize the root of the unstable mode and obtain the eigenvector as well. For the root location process, we do not have to employ classical complex root finding procedures such as Muller's deflation. The classical procedures would prove to be unreliable and erroneous, since the complex-valued determinant near the root has a highly irregular behavior.

The code is benchmarked and utilized in further analysis, and the results are discussed in the following section. Reasonable convergence of the eigenfrequencies can be achieved using 15–21 poloidal modes and 33 radial nodes with unequal spacing. The determinant evaluation takes about 5 s on a Cray-YMP/C90 processor for a set of 10 values, and the inverse iteration procedure takes about 15 s. The code is written in Fortran and is automatically vectorized. The library routines are optimized. We obtain an aggregate performance of about 340 Mflops using single tasking in a Cray-YMP/C90, which is about 34% of the theoretical speed of a single Cray-YMP/C90 processor.

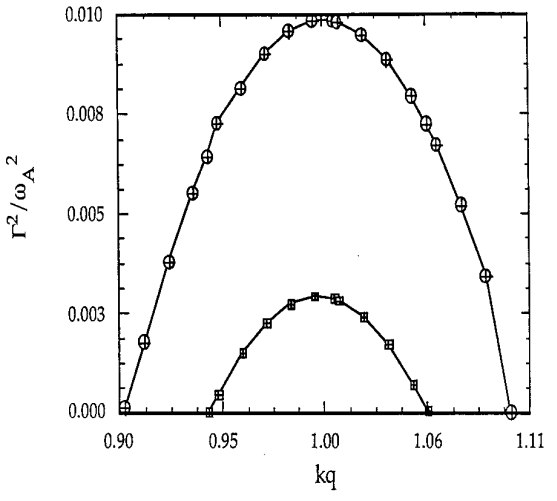

FIG. 2. Dependence of the square of growth rate on the product kq for two unstable $m = 1$ internal kink modes in a homogeneous cylinder.

RESULTS OF THE INSTABILITY CALCULATIONS

The computational procedures of the new code are benchmarked using published results of the internal kink

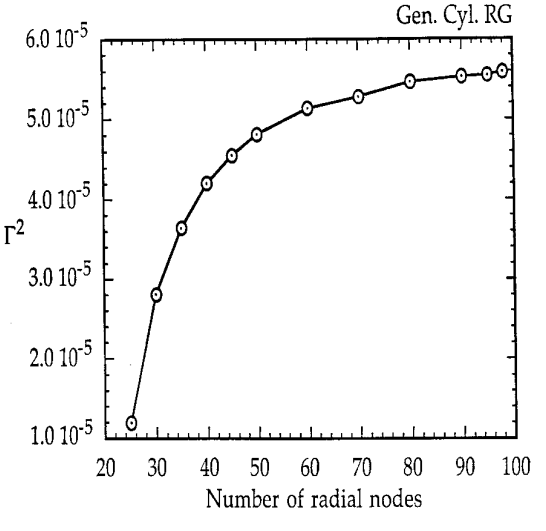

FIG. 3. Convergence of the square of the growth rate, Γ^2, with respect to radial nodes for the general cylindrical internal kink.

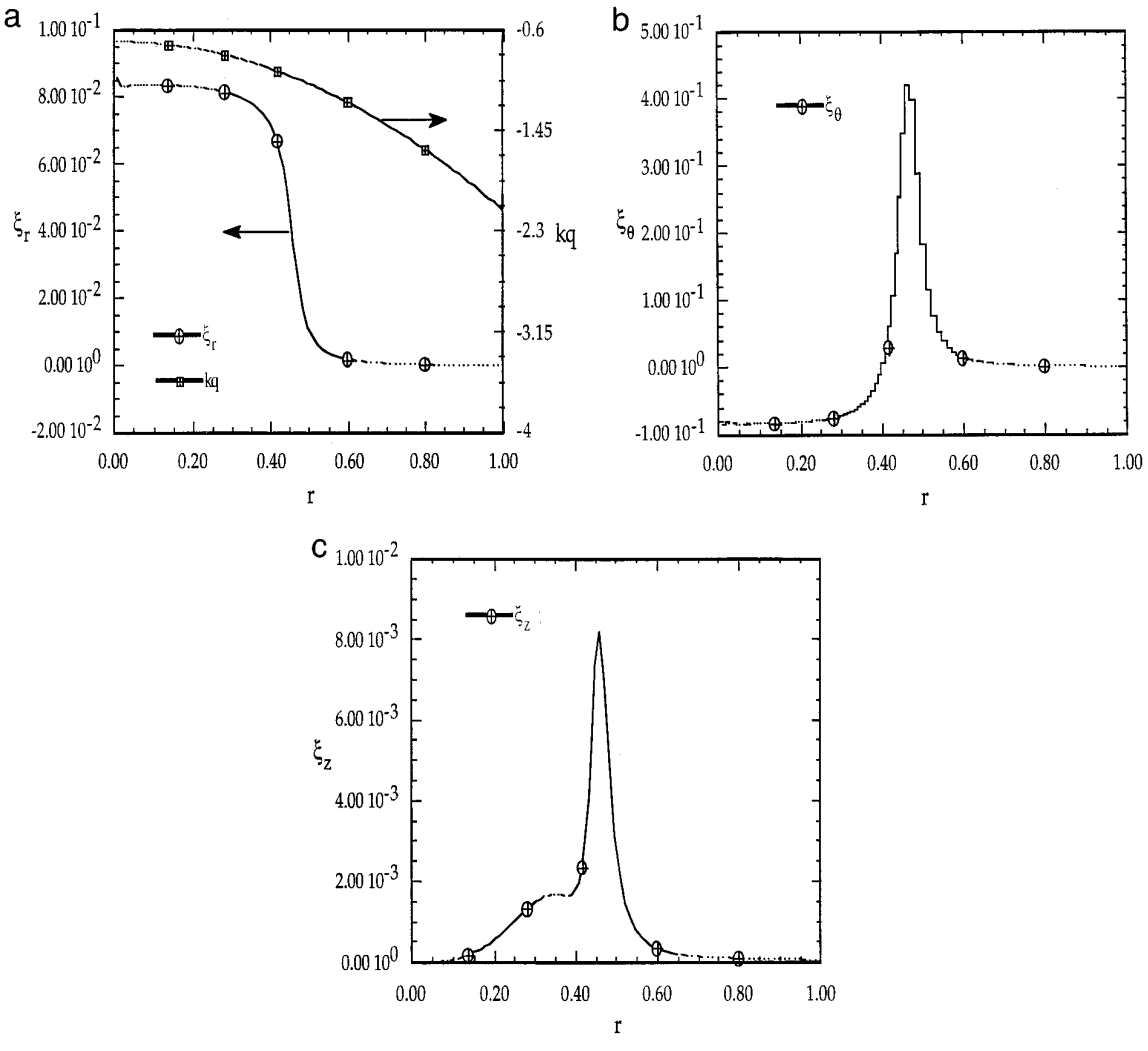

FIG. 4. a. Eigenfunction ξ_r and kq profile for the general cylindrical kink. b. Eigenfunction ξ_θ for the general cylindrical kink. c. Eigenfunction ξ_z for the general cylindrical kink.

mode eigenfrequency for two cylindrical instability problems and, also, by using $n = 2$ kink mode results for a Solovev equilibrium. For the two cylindrical problems, the static ideal MHD energy principle in cylindrical geometry is used to test the code integrity.

First, the results for the first two most unstable internal modes of a homogeneous thin cylinder problem [31, 42] are shown in Fig. 2. This configuration is cylindrical with

$$B(r) = (0, B_\theta, 1), \tag{47a}$$

$$j(r) = (0, 0, j_z), \tag{47b}$$

and $j_z(r)$ and $\rho(r)$ are constant; $\rho(r)$ is set to unity. When $F = \mathbf{k}\cdot\mathbf{B} = (m/r)B_\theta + kB_z$ vanishes, the internal kink instability arises. In this problem, around integer kq values, there are multiple internal modes for a given k.

TABLE I

Scaled Growth Rate Squared for Solovev Equilibrium

		Ω^2			
$q(0)$	$q(1)$	PINK	PEST	ERATO	Kerner
0.3	0.522	0.4018	0.427	0.431	0.413
0.7	1.219	0.118	0.119	0.120	0.118

Note. The eigenvalue ω^2 is given in terms of the poloidal Alfven time: $\Omega^2 = \omega^2[\rho q(1)^2 R^2/B_0^2]$ for $n = 2$ internal kink mode. The Solovev equilibrium with constant $F(=RB_\phi)$ is characterized by three parameters: ellipticity at axis E; q at axis $q(0)$; inverse aspect ratio parameter ε: $[2\psi_0 q(0)/ER^2B_0]^{1/2}$. For the table, $R = B_0 = 1$; $\rho = 1$, $\varepsilon = \frac{1}{3}$; $E = 2$.

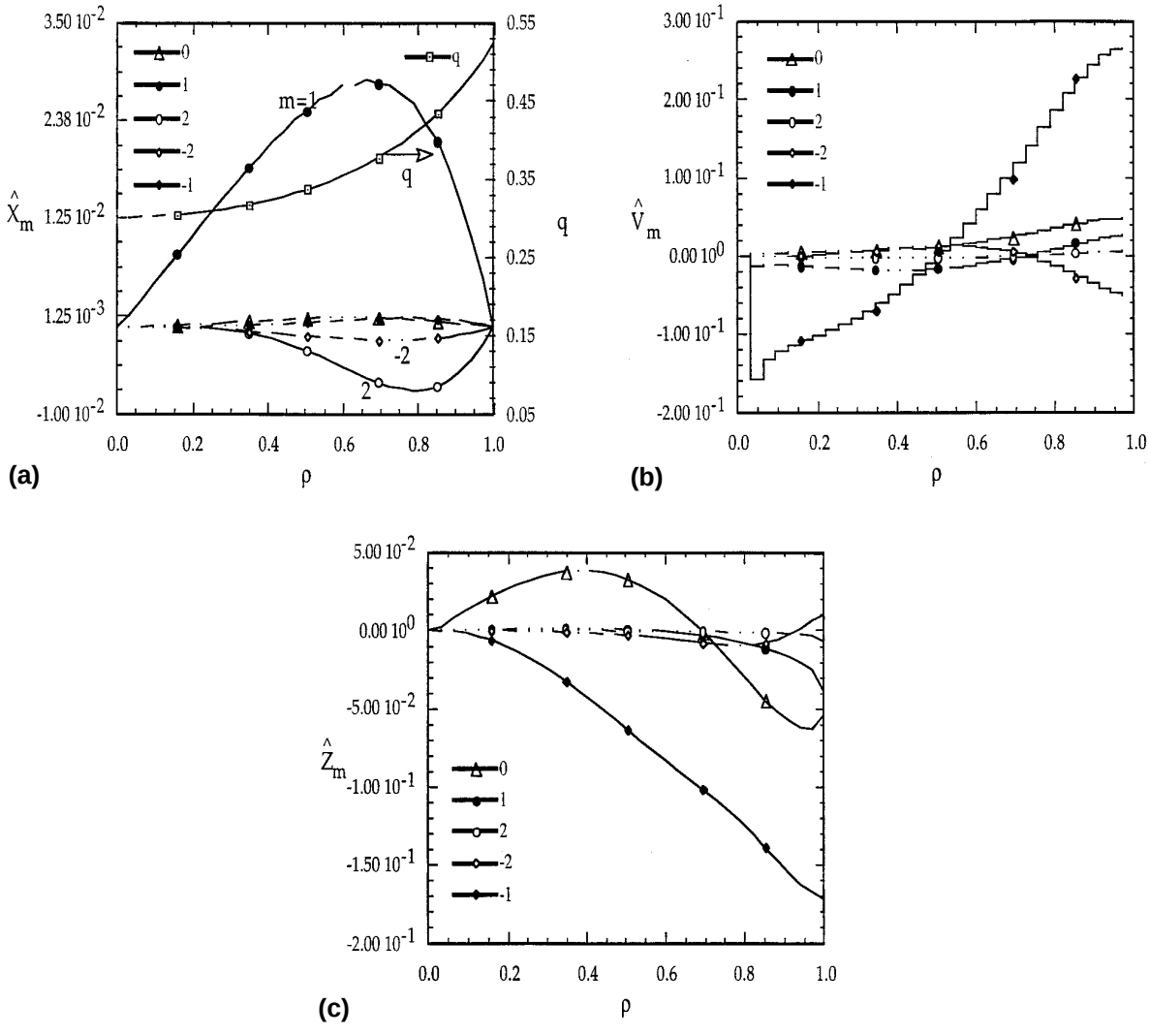

FIG. 5. a. Eigenmodes $\hat{X}$ for a representative Solovev equilibrium. b. Eigenmodes $\hat{V}$ for a representative Solovev equilibrium. c. Eigenmodes $\hat{Z}$ for a representative Solovev equilibrium.

Here q is the safety factor. The basic equilibrium is governed by

$$\frac{dp}{dr} + \frac{B_\theta}{r}\frac{d(rB_\theta)}{dr} + B_z\frac{dB_z}{dr} = 0, \tag{48}$$

and the profiles are

$$B_\theta = \tfrac{1}{2} j_z r, \tag{49a}$$

$$p = \tfrac{1}{4} j_z^2 (1 - r^2), \tag{49b}$$

the safety factor is

$$q = \frac{rB_z}{B_\theta} = \frac{2}{j_z} \tag{49c}$$

and the flux is

$$\psi(r) = -\tfrac{1}{4} j_z r^2. \tag{49d}$$

The instability growth rate is normalized with respect to the Alfven frequency given by $\omega_A^2 = k^2$. The results of the $m = 1$ mode produced in Fig. 2 are in excellent agreement with earlier published calculations [31].

Next, the results are obtained for an internal kink mode in a more general cylindrical equilibrium [31]. The equilibrium is described by

TABLE II

Parameters of Rotating ITER-like and TFTR-like Equilibria

Parameter	ITER-like	TFTR-like
R_0	7.0 m	2.4 m
Minor radius, a	2.0 m	0.7 m
R_{axis}	7.415 m	2.539 m
Ellipticity, κ	1.0	1.0
B_0	7 T	5 T
Ω_{tor}	0–100,000 rad/s	0–100,000 rad/s
$\langle\beta\rangle$	0.0255	0.019
I_p	10 MA	2.3 MA
$q(0)$, $q(1)$	0.857, 2.457	0.945, 2.659

Note. These equilibria were calculated with $p_2/p_1 = -0.2$, $t_1/p_1 = -20.0$, $t_2/p_1 = 4.0$, and $\rho(0)/p_1 = 3.0 \times 10^{-13}$. For the meaning of the parameters, see Appendix B.

$$\mathbf{B}(r) = \left(0, \frac{c_1 r}{1 + c_2^2 r^2}, 1\right), \tag{50}$$

and the pressure, q, and the flux profiles are given as

$$p(r) = \frac{c_1^2}{2c_2^2}\left[\frac{1}{(1 + c_2^2 r^2)^2} - \frac{1}{(1 + c_2^2 r^2)^2}\right], \tag{51a}$$

$$kq(r) = \frac{krB_z}{B_\theta} = \frac{1 + c_2^2 r^2}{c_1} k, \tag{51b}$$

$$\psi(r) = \frac{c_1}{2c_2^2} \ln (1 + c_2^2 r^2). \tag{51c}$$

This problem provides an interesting benchmark case. The $n = 1$ internal kink mode frequency converges slowly from

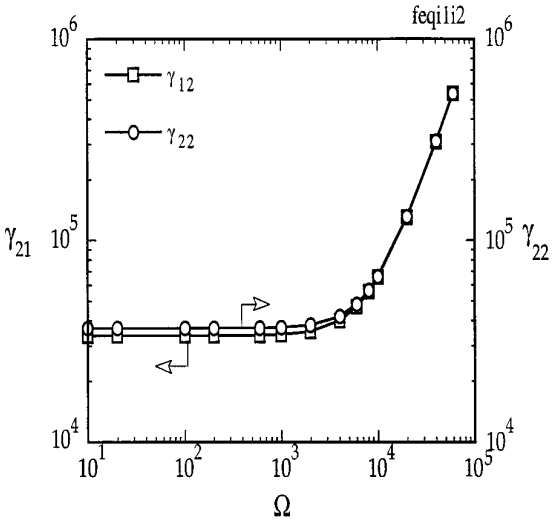

FIG. 7. Convergence of growth rates for two different FEM discretizations.

below the maximum growth rate to the asymptotic value of $\Gamma^2 = 5.9 \times 10^{-5}$. The growth rate convergence is achieved only for a large number of radial nodes, even with an uneven mesh; the convergence rate is shown in Fig. 3. The eigenfunctions are shown in Figs. 4a–c; their shapes are in very good agreement with the published results [31].

It is customary to benchmark plasma instability codes using the Solovev equilibrium [43]. Here, a comparison against the internal kink mode results for the Solovev equilibrium is given. The scaled values of γ^2 are indicated for

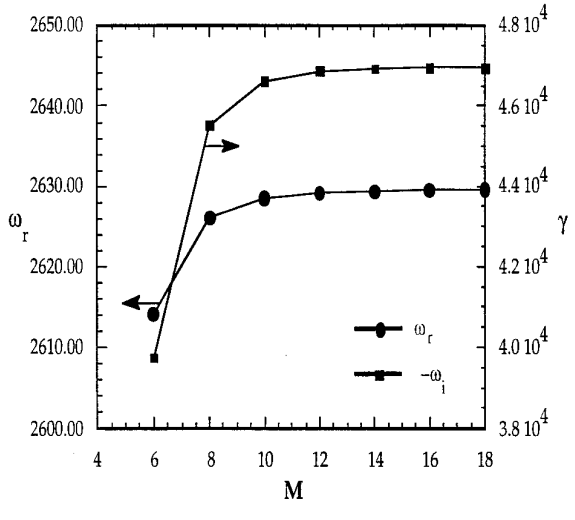

FIG. 6. Mode frequency and growth rate (ω_r, γ) versus poloidal modes for a differentially rotating equilibrium [$\Omega_{\text{tor,axis}} = 4000$].

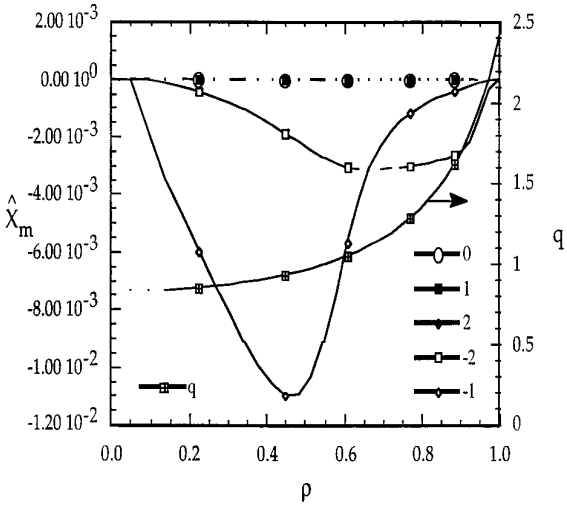

FIG. 8. Eigenmodes $\hat{X}$ for a rotating circular equilibrium [$\Omega_{\text{tor,axis}} = 4000$].

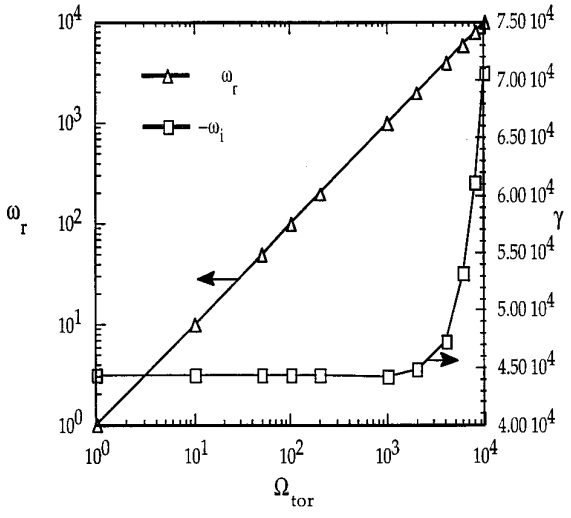

FIG. 9. Mode frequency and growth rate (ω_r, γ) versus toroidal rotation for a rigidly rotating equilibrium. The real part of ω is almost identical to the angular velocity Ω_{tor}!

two different $q(0)$ values given in Table I, where $q(0)$ is the safety factor at the magnetic axis. For the two cases where we could make a direct numerical comparison, the results compare well with the published data. The mode shapes obtained from the inverse iteration procedure for the three different radial eigenfunctions $\hat{X}$, $\hat{V}$, $\hat{Z}$ are given in Figs. 5a–c. These figures show the finite element approximations of the eigenfunctions. It should be noted that the $m = 1$ component is dominant. The square of the growth rate and the shape of the radial eigenfunctions for cylindrical, as well as for toroidal, geometry agree with the previous results. The agreement with prior results presented so far indicates that radial discretization with 33 nonuniformly spaced nodes yields acceptable convergence of the growth rates.

The central objective of this paper is to estimate the growth rates of the most unstable kink mode in a rotating plasma. We have limited our analysis to the toroidal rotation only. Once a more general quadratic form of the force operator is derived, including equilibrium poloidal flows, the stability of elliptic flow equilibria can be analyzed.

It should be noted that the standard workhorse tokamak MHD codes do not have a provision for including plasma rotation effects, since they generally solve the self-adjoint MHD energy principle of Bernstein *et al.* [1] However, as emphasized in the introduction, plasma rotation plays a key role in characterizing the mode shapes and eigenfrequencies, and the presence of rotational instabilities can be experimentally observed. For example, the $\dot{b}_\theta$ signals from the Rogowski coils frequently exhibit a "fishbone"-like oscillation [44], and this instability is frequently present along with a low-mode-number rotating internal kink mode. As a result, the mode frequencies of the rotating unstable kinks can be experimentally extracted from the signals of the field perturbations registered by Rogowski coils.

In the computational results presented here, we consider fixed boundary axisymmetric equilibria similar to the international thermonuclear experimental reactor (ITER)-like and the tokamak fusion test reactor (TFTR). Some of the assumed parameters of the equilibria are summarized in Table II. Both these equilibria are assumed to have circular cross sections. The equilibria are computed using a simple toroidal flow equilibrium model and are solved by a multigrid method. Some details of the equilibrium flux calculations are furnished in Appendix B. The toroidal rotational velocities and the specified density and pressure profiles constitute only a subsonic system. The plasma density is specified at the center to be about 2×10^{-13} kg/m^3 and the center pressure is about 10^6 N/m^2. One can verify that Mach number $\mathcal{M} = v/C_s \ll 1$ for these parameters in the core region of the plasma, where the sound speed C_s is given by $\sqrt{\gamma p/\rho}$.

The results for the complex mode frequencies of the most unstable internal kink modes show that the real part of the mode frequency scales linearly with plasma rotation and that the growth rate varies nonlinearly with rotation. The growth rate convergence with respect to total poloidal modes is illustrated in Fig. 6. The nonuniformly spaced radial discretization used in the static MHD analysis is also retained for obtaining the growth rates of the flow equilibria. A comparison of the calculated eigenfrequencies for two different *radial* discretizations is illustrated in Fig. 7. This comparison shows that the problem under consideration here has convergent mode frequencies and mode shapes with the chosen FEM discretization. We have prescribed a roof function for $\hat{X}$, a tent function for $\hat{V}$, and either a roof or a tent function for $\hat{Z}$ for the results in Fig. 7. We obtain essentially convergent results for these two different FEM representations of $\hat{Z}$. Other combinations do not give the same results, even for Solovev or static equilibria; hence we do not consider their results as relevant.

The radial eigenfunction is illustrated in Fig. 8. The real part and the imaginary part of the eigenfrequency are plotted with respect to the *rigid* toroidal rotation in Fig. 9. The real part of the mode frequency is the same as the toroidal rotation frequency. This is to be expected for rigid body rotation. The growth rate of the unstable mode increases rapidly at higher toroidal rotation. The eigenfunctions show sharp variation around the critical surface, and one such result is shown using a projection of the perturbed vector in $\phi = 0$ plane in Fig. 10.

In practical tokamak plasmas, the edge velocities tend to be much smaller than the central velocities. Thus the

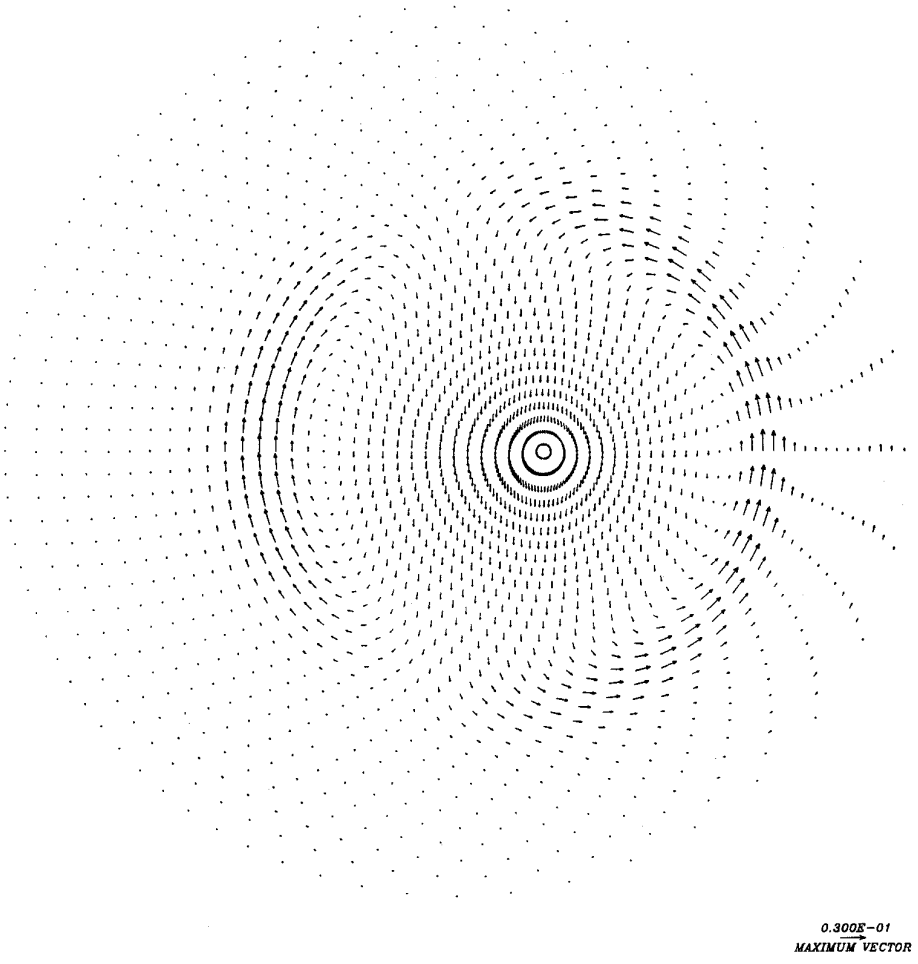

FIG. 10. Projection of perturbation vector on $\phi = 0$ for a rotating equilibrium.

case of *differential* rotation is of significant interest. In many situations, the incipient values of the mode rotation frequencies can be identified and related to the plasma differential rotation. A case with differential rotation, given by $\Omega_0[1 - (\psi/\psi_0)^2]$, has been examined. It exhibits real part and growth rate similar to the case of rigid body rotation, and it is illustrated in Fig. 11. The magnitudes of these values are less for this case, compared to rigid body rotation with the same peak velocity.

From the rapidly increasing growth rate at large toroidal rotation frequencies, we can surmise that a mode can become unstable, even when the axis safety factor is above unity. For an axis safety factor well above unity, instability would be observed at high plasma rotation, since the rotational energy arising from the Hermitian part, namely, $\int d^3\mathbf{x}\boldsymbol{\xi}^* \cdot \mathbf{F}(\boldsymbol{\xi})$, can drive the stable modes unstable at high rotational frequencies, by making $\int d^3\mathbf{x}\boldsymbol{\xi}^* \cdot \mathbf{F}(\boldsymbol{\xi}) > 0$. An illustration of this case is given in Fig. 12. The mode is stable against plasma rotation up to about 29000 rad/s. For higher rotational velocities, the growth rate is nonzero, and the mode is clearly unstable. The perturbations resemble an internal kink.

Similar results are shown in Figs. 13, 14 for a TFTR-like equilibrium. In Fig. 13, the kink is already unstable, since $q_0 < 1$, and rotation further destabilizes the mode. In Fig. 14, a stable kink with $q_0 > 1$ is destabilized at high rotation velocities represented by larger Ω values. The kinetic energy of the plasma is very small for the configurations illustrated here, yet the plasma modes can be destabilized at rotation velocities that are still in the low end of the subsonic regime. The kink modes shown in Figs. 11–14 are drived increasingly unstable at higher toroidal plasma rotation rates due to increasing centrifugal forces. Thus we have labeled these modes as "centrifugally destabilized internal kinks."

Since the representative plasma angular rotation rates, used in this paper to illustrate the centrifugal instability, are often observed in contemporary tokamak discharges, it is likely that this rotational kink mode can be identified and characterized appropriately. The oscillations would

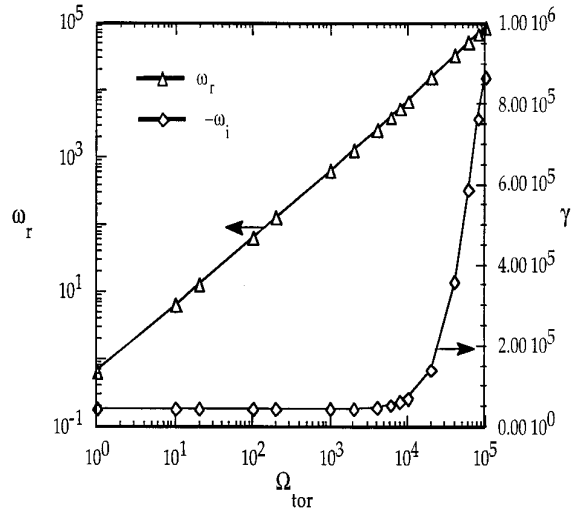

FIG. 11. Mode frequency and growth rate (ω_r, γ) versus toroidal rotation of a differentially rotating ITER-like equilibrium; real part ω_r varies linearly with the center angular velocity Ω_{tor}.

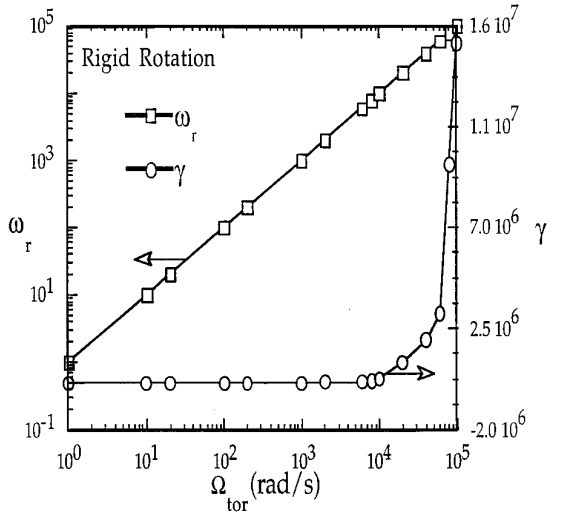

FIG. 13. Mode frequency and growth rate (ω_r, γ) of an unstable $n = 1$ kink in a TFTR-like equilibrium (Table II) equilibrium for $q_0 = 0.945$.

resemble the slow mode accompanying the ''fishbone''-like oscillations. However, the rotating internal kinks can also become resonant at trapped particle magnetic precession frequencies in beam-injected plasmas and resemble a ''fishbone'' mode, thus complicating the interpretation of the mode characteristics. In this situation, additional non-adiabatic hot ion contributions could be added to solve for the improved mode frequencies [44]. But the basic destabilization of the mode with plasma rotation is likely to be generally observable, especially as a slow continuous mode reported in Ref. [44].

The rotational modes can be further characterized by varying some significant plasma parameters, such as the plasma major radius, axial magnetic field, plasma ellipticity, and q_0. Such results are given elsewhere [34]. The main observations are that the mode growth rate increases with the plasma aspect ratio and decreases with ellipticity. The real part of the mode frequency scales linearly with toroidal rotation for all plasma size and shape parameters.

CONCLUSIONS

It has been demonstrated that the mode frequencies of the unstable linear internal kink modes with toroidal

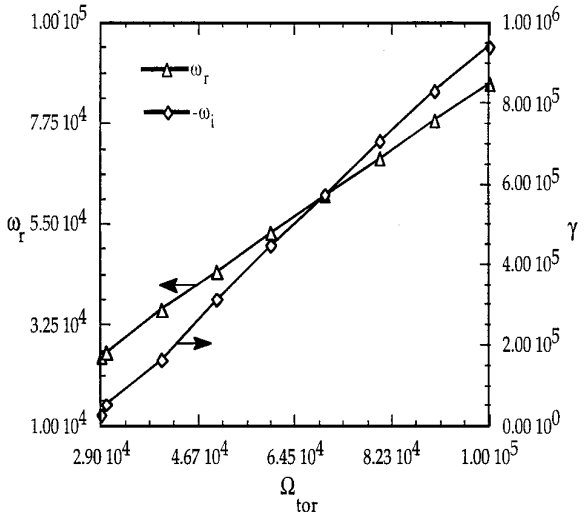

FIG. 12. Frequency versus rotation of a destabilized $n = 1$ kink for an ITER-like (Table II) equilibrium.

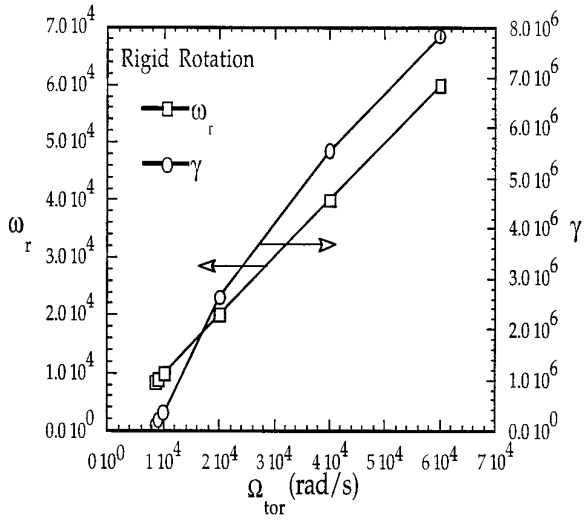

FIG. 14. Mode frequency and growth rate (ω_r, γ) of an unstable $n = 1$ kink in a TFTR-like equilibrium (Table II) equilibrium for $q_0 = 1.05$.

rotation in the low-end subsonic regime can be characterized by numerically solving the Frieman–Rotenberg equation. Plasma rotation strongly increases the growth rate of the unstable $n = 1$ internal kink when the axis safety factor is below unity. This internal kink can also be destabilized at high rotational velocities when the axis safety factor is above unity. The real part linearly scales with the plasma rotation.

These characteristics define centrifugally destabilized internal kinks, which have been observed in contemporary tokamaks as well as in astrophysical objects. Also, the plasma internal modes, such as "fishbone" and toroidal Alfven eigen (TAE) modes, can be better characterized by including toroidal rotation in linear instability analysis, since they contain strong destabilization factors arising from plasma rotation.

The manifestly self-adjoint form of the force operator in the Frieman–Rotenberg equations has been shown here for the case of finite toroidal rotation, and it is cast in the form closely resembling the force operator in static MHD analysis, familiar to computational researchers in plasma physics. This form could thus be used in the workhorse MHD codes, and the methods demonstrated here could be routinely utilized in these codes to study the effect of plasma rotation. Plasma stability boundaries should be revised to accommodate high plasma rotation velocities observed in tokamaks.

In this paper, the influence of strong poloidal flows observed in tokamak discharges has not been modelled. The poloidal flows are thought to be responsible for various stabilization mechanisms that result in L to H transition in confinement regimes. A consistent stability analysis including strong toroidal and poloidal flow profiles in tokamaks could be undertaken, using generalized variational procedures starting from the Frieman–Rotenberg equation. However, this could be very complicated and various nonlinear numerical studies pertaining to tokamak poloidal flows already exist. Linear stability analysis would be useful in design optimization procedures, since nonlinear studies require much longer computational times.

APPENDIX A: COMPUTATIONAL FORM OF EQ. (31)

First the terms in Eq. (31) are tagged, and the equation is written out as

$$
\begin{aligned}
&\omega^2 \overset{\boxed{1}}{\int d^3x\rho\boldsymbol{\xi}^*\cdot\boldsymbol{\xi}} + 2i\omega \overset{\boxed{2}}{\int d^3x \times \boldsymbol{\xi}^*\cdot(\rho\mathbf{v}\cdot\nabla\boldsymbol{\xi})} \\
&= \int d^3x \Bigg\{ \overset{\boxed{3}}{\gamma p|\nabla\cdot\boldsymbol{\xi}|^2} + \overset{\boxed{4}}{\left|\mathbf{Q} + \frac{\boldsymbol{\xi}\cdot\nabla\psi}{|\nabla\psi|^2} J\times\nabla\psi\right|^2} - \overset{\boxed{5}}{2\,\nabla\psi\cdot\boldsymbol{\kappa}\frac{|\boldsymbol{\xi}\cdot\nabla\psi|^2}{|\nabla\psi|^2}\frac{\nabla\psi\cdot\nabla p}{|\nabla\psi|^2}} \\
&\quad + \overset{\boxed{6}}{S\frac{\mathbf{B}\cdot\mathbf{J}}{B^2}|\boldsymbol{\xi}\cdot\nabla\psi|^2} - \overset{\boxed{7}}{\frac{|\boldsymbol{\xi}\cdot\nabla\psi|^2}{|\nabla\psi|^2}\left(\frac{\mathbf{J}\cdot\mathbf{B}}{B}\right)^2} - \overset{\boxed{8}}{2\,\nabla\psi\cdot\boldsymbol{\kappa}\frac{|\boldsymbol{\xi}\cdot\nabla\psi|^2}{|\nabla\psi|^2}\frac{\nabla\psi\cdot(\rho\mathbf{v}\cdot\nabla\mathbf{v})}{|\nabla\psi|^2}} \\
&\quad - \overset{\boxed{9}}{\boldsymbol{\xi}\cdot(\rho\mathbf{v}\cdot\nabla\mathbf{v})\nabla\cdot\boldsymbol{\xi}^*} - \overset{\boxed{10}}{\boldsymbol{\xi}^*\cdot(\rho\mathbf{v}\cdot\nabla\mathbf{v})\nabla\cdot\boldsymbol{\xi}} - \overset{\boxed{11}}{\rho|\mathbf{v}\cdot\nabla\boldsymbol{\xi}|^2} + \overset{\boxed{12}}{\boldsymbol{\xi}^*\cdot(\boldsymbol{\xi}\cdot\nabla)\,\nabla p} \\
&\quad - \overset{\boxed{13}}{\boldsymbol{\xi}^*\cdot\nabla\psi\,\boldsymbol{\xi}\cdot\nabla\left(\frac{\nabla\psi\cdot\mathbf{J}\times\mathbf{B}}{|\nabla\psi|^2}\right)} - \overset{\boxed{14}}{\boldsymbol{\xi}\cdot\nabla\psi\,\boldsymbol{\xi}^*\cdot\nabla\left(\frac{\nabla\psi\cdot\mathbf{J}\times\mathbf{B}}{|\nabla\psi|^2}\right)} - \overset{\boxed{15}}{\boldsymbol{\xi}^*\cdot(\boldsymbol{\xi}\cdot\nabla)\nabla\psi\frac{\nabla\psi\cdot\mathbf{J}\times\mathbf{B}}{|\nabla\psi|^2}} \\
&\quad + \overset{\boxed{16}}{\frac{|\boldsymbol{\xi}\cdot\nabla\psi|^2}{|\nabla\psi|^2}\nabla\psi\cdot\nabla\left(\frac{\nabla\psi\cdot\mathbf{J}\times\mathbf{B}}{|\nabla\psi|^2}\right)}\Bigg\}.
\end{aligned}
\tag{A1}
$$

In Eq. (A1), $\boldsymbol{\kappa}$ is the curvature $\mathbf{b}.\nabla\mathbf{b}$, and the local shear S is given by

$$S = \frac{\mathbf{B}\times\nabla\psi}{|\nabla\psi|^2}\cdot\nabla\times\left(\frac{\mathbf{B}\times\nabla\psi}{|\nabla\psi|^2}\right).$$

The individual components are calculated as follows. First, a new flux surface variable "s" is introduced as

$$s = \sqrt{\psi/\psi_0}. \tag{A2}$$

Then the radial ψ derivative becomes

$$\frac{\partial}{\partial\psi} = \frac{1}{2s\psi_0}\frac{\partial}{\partial s}. \tag{A3}$$

All the scalar components X, V, and Z of $\boldsymbol{\xi}$ are written in terms of new variables $\hat{X}$, $\hat{V}$, and $\hat{Z}$:

$$\hat{X} = X, \tag{A4}$$

$$\hat{V} = 2s\psi_0, \tag{A5}$$

$$\hat{Z} = 2s\psi_0 Z. \tag{A6}$$

With this introduction of new variables, the individual terms in the bilinear form in Eq. (A1) are written in the scalar form. In the following the inverse of the Jacobian is $\mathscr{J}^{-1} = \nabla\phi\times\nabla\psi\cdot\nabla\theta$. The expressions for the individual terms are derived using the projection approach employed in the ERATO code.

The $\delta\mathbf{B}$ is calculated as

$$\nabla\times(\boldsymbol{\xi}\times\mathbf{B}) + \frac{\nabla\psi\cdot\boldsymbol{\xi}\,\mathbf{J}\times\nabla\psi}{|\nabla\psi|}\frac{\mathbf{J}\times\nabla\psi}{|\nabla\psi|} = A_1\frac{\nabla\psi}{|\nabla\psi|} + A_2\frac{\nabla\phi}{|\nabla\phi|} + A_3\frac{\nabla\phi\times\nabla\psi}{|\nabla\phi|\,|\nabla\psi|}, \tag{A7}$$

where

$$A_1 = \frac{\mathscr{J}^{-1}}{|\nabla\psi|}\left[\left(\frac{2RR_\theta}{\mathscr{J}} - \frac{R^2}{\mathscr{J}^2}\mathscr{J}_\theta\right)X + \frac{R^2}{\mathscr{J}}X_\theta + JX_\phi\right]$$
$$= \frac{\mathscr{J}^{-1}}{|\nabla\psi|}\left[\left(\frac{2RR_\theta}{\mathscr{J}} - \frac{R^2}{\mathscr{J}^2}\mathscr{J}_\theta\right)\hat{X} + \frac{R^2}{\mathscr{J}}\hat{X}_\theta + J\hat{X}_\phi\right], \tag{A8}$$

$$A_2 = \frac{JR}{\mathscr{J}}[X_\psi + V_\theta]$$
$$= \frac{JR}{2s\psi_0\,\mathscr{J}}[\hat{X}_s + \hat{V}_\theta], \tag{A9}$$

$$A_3 = \left[-\frac{|\nabla\psi|}{R}\left(\frac{2RR_\psi}{\mathscr{J}} - \frac{R^2}{\mathscr{J}^2}\mathscr{J}_\psi\right) - \frac{\nabla\psi\cdot\nabla\theta}{R|\nabla\psi|}\left(\frac{2RR_\theta}{\mathscr{J}} - \frac{R^2}{\mathscr{J}^2}\mathscr{J}_\theta\right) + \frac{R}{\mathscr{J}|\nabla\psi|}\Delta^*\psi\right]X - \frac{|\nabla\psi|R}{\mathscr{J}}X_\psi - \frac{\nabla\psi\cdot\nabla\theta R}{|\nabla\psi|\,\mathscr{J}}X_\theta$$
$$- \frac{\nabla\psi\cdot\nabla\theta J}{|\nabla\psi|R}X_\phi + \frac{|\nabla\psi|J}{R}V_\phi = \frac{1}{2s\psi_0}$$
$$\times\left\{\left[-\frac{|\nabla\psi|}{R}\left(\frac{2RR_s}{\mathscr{J}} - \frac{R^2}{\mathscr{J}^2}\mathscr{J}_s\right) - 2s\psi_0\frac{\nabla\psi\cdot\nabla\theta}{R|\nabla\psi|}\right.\right.$$
$$\left.\times\left(\frac{2RR_\theta}{\mathscr{J}} - \frac{R^2}{\mathscr{J}^2}\mathscr{J}_\theta\right) + 2s\psi_0\frac{R}{\mathscr{J}|\nabla\psi|}\Delta^*\psi\right]\hat{X} - \frac{|\nabla\psi|R}{\mathscr{J}}\hat{X}_s$$
$$\left. - 2s\psi_0\frac{\nabla\psi\cdot\nabla\theta R}{|\nabla\psi|\,\mathscr{J}}\hat{X}_\theta - 2s\psi_0\frac{\nabla\psi\cdot\nabla\theta J}{|\nabla\psi|R}\hat{X}_\phi + \frac{|\nabla\psi|J}{R}\hat{V}_\phi\right\}. \tag{A10}$$

Also $\nabla\cdot\boldsymbol{\xi}$ can be written as

$$\begin{aligned}\nabla\cdot\boldsymbol{\xi} &= \mathscr{J}^{-1}[R^2X_\psi + 2RR_\psi X] + \mathscr{J}^{-1}[R^2V_\theta + 2RR_\theta V] \\ &\quad + \mathscr{J}^{-1}[R^2Z_\theta + 2RR_\theta Z] + JZ_\phi \\ &= \frac{\mathscr{J}^{-1}}{2s\psi_0}[R^2\hat{X}_s + 2RR_s\hat{X}] + \frac{\mathscr{J}^{-1}}{2s\psi_0}[R^2\hat{V}_\theta + 2RR_\theta\hat{V}] \\ &\quad + \frac{\mathscr{J}^{-1}}{2s\psi_0}[R^2\hat{Z}_\theta + 2RR_\theta\hat{Z}] + \frac{J}{2s\psi_0}\hat{Z}_\phi.\end{aligned} \tag{A11}$$

To calculate the kinetic energy term, $\boldsymbol{\xi}$ is projected as

$$\boldsymbol{\xi} = B_1\frac{\nabla\psi}{|\nabla\psi|} + B_2\frac{\nabla\phi}{|\nabla\phi|} + B_3\frac{\nabla\phi\times\nabla\psi}{|\nabla\phi|\,|\nabla\psi|}, \tag{A12}$$

where

$$B_1 = \frac{XR^2}{\mathscr{J}|\nabla\psi|} = \frac{\hat{X}R^2}{\mathscr{J}|\nabla\psi|}, \tag{A13}$$

$$B_2 = JRZ = \frac{JR}{2s\psi_0}\hat{Z}, \tag{A14}$$

$$\begin{aligned}B_3 &= -\frac{\nabla\psi\cdot\nabla\theta}{|\nabla\psi|}RX + |\nabla\psi|RV + |\nabla\psi|RZ \\ &= \frac{|\nabla\psi|R}{2s\psi_0}\left\{-\frac{\nabla\psi\cdot\nabla\theta}{|\nabla\psi|^2}2s\psi_0\hat{X} + \hat{V} + \hat{Z}\right\}.\end{aligned} \tag{A15}$$

The kinetic energy term $\boxed{1}$ is written finally as

$$\int d^3x\rho\xi^2 = \int ds\,d\theta\,\mathscr{J}2s\psi_0\rho\left\{\frac{R^4}{\mathscr{J}^2|\nabla\psi|^2}\hat{X}\hat{X}^* + \frac{J^2R^2}{4s^2\psi_0^2}\hat{Z}\hat{Z}^*\right.$$
$$\left. + \frac{R^2|\nabla\psi|^2}{4s\psi_0^2}\left|-\frac{\nabla\psi\cdot\nabla\theta}{|\nabla\psi|^2}2s\psi_0\hat{X} + \hat{V} + \hat{Z}\right|^2\right\}. \tag{A16}$$

Terms involving $\mathbf{v}\cdot\nabla\boldsymbol{\xi}$ are calculated after orthogonally projecting $\mathbf{v}\cdot\nabla\boldsymbol{\xi}$ as

$$\mathbf{v}\cdot\nabla\boldsymbol{\xi} = C_1\frac{\nabla\psi}{|\nabla\psi|} + C_2\frac{\nabla\phi}{|\nabla\phi|} + C_3\frac{\nabla\phi\times\nabla\psi}{|\nabla\phi|\,|\nabla\psi|}, \quad \text{(A17)}$$

where

$$C_1 = -\frac{\Omega RJ\psi_R}{|\nabla\psi|}Z + \frac{\Omega R^2\mathscr{J}^{-1}}{|\nabla\psi|}X_\phi$$
$$= -\frac{\Omega RJ\psi_R}{2s\psi_0|\nabla\psi|}\hat{Z} + \frac{\Omega R^2\mathscr{J}^{-1}}{|\nabla\psi|}\hat{X}_\phi, \quad \text{(A18)}$$

$$C_2 = \Omega[-\theta_z RX + \psi_z RV + \psi_z RZ) + \Omega JRZ_\phi = \frac{\Omega}{2s\psi_0}$$
$$\times[-2s\psi_0\theta_z R\hat{X} + \psi_z R\hat{V} + \psi_z R\hat{Z}] + \frac{\Omega JR}{2s\psi_0}\hat{Z}_\phi, \quad \text{(A19)}$$

$$C_3 = -\frac{\Omega R^2J\mathscr{J}^{-1}R_\theta}{|\nabla\psi|}Z + \Omega R|\nabla\psi|$$
$$\times\left[-\frac{\nabla\psi\cdot\nabla\theta}{|\nabla\psi|^2}X_\phi + V_\phi + Z_\phi\right]$$
$$= -\frac{\Omega R^2J\mathscr{J}^{-1}R_\theta}{2s\psi_0|\nabla\psi|}\hat{Z} + \frac{\Omega R|\nabla\psi|}{2s\psi_0}$$
$$\times\left[-\frac{\nabla\psi\cdot\nabla\theta}{|\nabla\psi|^2}2s\psi_0\hat{X}_\phi + \hat{V}_\phi + \hat{Z}_\phi\right]. \quad \text{(A20)}$$

Then the nonhermitian component numbered 2 on the left-hand side of (A.1) is expanded as

$$\int d^3x\boldsymbol{\xi}^*\cdot(\rho\mathbf{v}\cdot\nabla\boldsymbol{\xi}) = \int ds\,d\theta\,2s\psi_0\mathscr{J}$$
$$\times\left\{\rho\frac{R^2\mathscr{J}^{-1}}{|\nabla\psi|^2 2s\psi_0}\hat{X}^*[-R\Omega]\psi_R\hat{Z} + \Omega R^2\mathscr{J}^{-1}2s\psi_0\hat{X}_\phi]\right.$$
$$-\rho R\frac{\nabla\psi\cdot\nabla\theta}{|\nabla\psi|}\hat{X}^*\left[\frac{\Omega R|\nabla\psi|}{2s\psi_0}\right.$$
$$\left.\times\left(-2s\psi_0\frac{\nabla\psi\cdot\nabla\theta}{|\nabla\psi|^2}\hat{X}_\phi + \hat{V}_\phi + \hat{Z}_\phi\right) - \frac{\Omega R^2J\mathscr{J}^{-1}R_\theta}{|\nabla\psi|2s\psi_0}\hat{Z}\right]$$
$$+\rho R\frac{|\nabla\psi|}{2s\psi_0}\hat{V}^*\left[\frac{\Omega R|\nabla\psi|}{2s\psi_0}\right. \quad \text{(A21)}$$
$$\times\left(-2s\psi_0\frac{\nabla\psi\cdot\nabla\theta}{|\nabla\psi|^2}\hat{X}_\phi + \hat{V}_\phi + \hat{Z}_\phi\right)$$
$$\left.-\frac{\Omega R^2J\mathscr{J}^{-1}R_\theta}{|\nabla\psi|2s\psi_0}\hat{Z}\right] + \rho\frac{RJ}{2s\psi_0}\hat{Z}^*$$
$$\times\left[\frac{\Omega RJ}{2s\psi_0}\hat{Z}_\phi + \Omega\left(-\theta_z R\hat{X} + \frac{\psi_z R}{2s\psi_0}\hat{V} + \frac{R\psi_z}{2s\psi_0}\hat{Z}\right)\right]$$
$$+\rho\frac{R|\nabla\psi|}{2s\psi_0}\hat{Z}^*\left[\frac{\Omega R|\nabla\psi|}{2s\psi_0}\right.$$
$$\left.\left.\times\left(-2s\psi_0\frac{\nabla\psi\cdot\nabla\theta}{|\nabla\psi|^2}\hat{X}_\phi + \hat{V}_\phi + \hat{Z}_\phi\right) - \frac{\Omega R^2J\mathscr{J}^{-1}R_\theta}{|\nabla\psi|2s\psi_0}\hat{Z}\right]\right\}.$$

The pressure and compressibility term tagged 3 on the r.h.s. is written as

$$\int d^3x\,\gamma p|\nabla\cdot\boldsymbol{\xi}|^2 = \int ds\,d\theta\,2s\psi_0\mathscr{J}\left\{\gamma p\frac{R^4}{\mathscr{J}^2 4s^2\psi_0^2}\left|\frac{2RR_s}{R^2}\hat{X}\right.\right.$$
$$\left.\left.+\frac{2RR_\theta}{R^2}\hat{V} + \frac{2RR_\theta}{R^2}\hat{Z} + \hat{X}_s + \hat{V}_\theta + \hat{Z}_\theta + \frac{J\mathscr{J}}{R^2}\hat{Z}_\phi\right|^2\right\}. \quad \text{(A22)}$$

The term tagged 4 containing the field perturbation term can be written as

$$\int d^3x\left|\mathbf{Q} + \frac{\boldsymbol{\xi}\cdot\nabla\psi}{|\nabla\psi|^2}J\times\nabla\psi|^2 = \int ds\,d\theta\,2s\psi_0\mathscr{J}\{A_1^2 + A_2^2 + A_3^2\right\}$$
$$= \int ds\,d\theta\,2s\psi_0\mathscr{J}$$
$$\times\left\{\frac{R^4}{|\nabla\psi|^2\mathscr{J}^4}\left|\frac{\mathscr{J}}{R^2}\left(\frac{2RR_\theta}{\mathscr{J}} - \frac{R^2}{\mathscr{J}^2}\mathscr{J}_\theta\right)\hat{X} + \hat{X}_\theta\right.\right.$$
$$\left.+\frac{J\mathscr{J}}{R^2}\hat{X}_\phi\right|^2 + \frac{R^2J^2}{4s^2\psi_0^2\mathscr{J}^2}|\hat{X}_s + \hat{V}_\theta|^2 \quad \text{(A23)}$$
$$+\frac{|\nabla\psi|^2R^2}{4s^2\psi_0^2\mathscr{J}^2}\left|\left[\frac{\mathscr{J}}{R^2}\left(\frac{2RR_s}{\mathscr{J}} - \frac{R^2}{\mathscr{J}^2}\mathscr{J}_s\right)\right.\right.$$
$$\left.+\frac{\nabla\psi\cdot\nabla\theta}{|\nabla\psi|^2}\frac{J}{R^2}\left(\frac{2RR_\theta}{\mathscr{J}} - \frac{R^2}{\mathscr{J}^2}\mathscr{J}_\theta\right)2s\psi_0 - \frac{2s\psi_0\Delta^*\psi}{|\nabla\psi|^2}\right]\hat{X}$$
$$\left.\left.+\hat{X}_s + \frac{\nabla\psi\cdot\nabla\theta}{|\nabla\psi|^2}2s\psi_0\left[\hat{X}_\theta + \frac{J\mathscr{J}}{R^2}\hat{X}_\phi\right] - \frac{J\mathscr{J}}{R^2}\hat{V}_\phi\right|^2\right\}.$$

The terms tagged 5, 6, and 7 are combined as

$$\int d^3x\left\{-2\,\nabla\psi\cdot\boldsymbol{\kappa}\frac{|\boldsymbol{\xi}\cdot\nabla\psi|^2}{|\nabla\psi|^2}\frac{\nabla\psi\cdot\nabla p}{|\nabla\psi|^2} + S\frac{\mathbf{B}\cdot\mathrm{J}}{B^2}|\boldsymbol{\xi}\cdot\nabla\psi|^2\right.$$
$$\left.-\frac{|\boldsymbol{\xi}\cdot\nabla\psi|^2}{|\nabla\psi|^2}\left(\frac{\mathbf{J}\cdot\mathbf{B}}{B}\right)^2\right\} = \int ds\,d\theta\,2s\psi_0\mathscr{J} \quad \text{(A24)}$$
$$\times\left\{\left\{-2\,\nabla\psi\cdot\boldsymbol{\kappa}\frac{\nabla\psi\cdot\nabla p}{|\nabla\psi|^2} + S\frac{\mathbf{B}\cdot\mathbf{J}}{B^2}|\nabla\psi|^2\right.\right.$$

$$- \left(\frac{\mathbf{J}\cdot\mathbf{B}}{B}\right)^2\Bigg\}\frac{R^4}{|\nabla\psi|^2\mathscr{J}^2}\hat{X}\hat{X}^*\Bigg\}.$$

With $\rho\mathbf{v}\cdot\nabla\mathbf{v} = -\rho\Omega^2 R\,\nabla R$, the terms tagged 8 through 16 are written as follows:

The term tagged 8 is written as

$$\int d^3x\left[-2\,\nabla\psi\cdot\boldsymbol{\kappa}\frac{|\boldsymbol{\xi}\cdot\nabla\psi|^2}{|\nabla\psi|^2}\frac{\nabla\psi\cdot(\rho\mathbf{v}\cdot\nabla\mathbf{v})}{|\nabla\psi|^2}\right] = \int ds\,d\theta\,2s\psi_0\mathscr{J} \times\left\{2\,\nabla\psi\cdot\boldsymbol{\kappa}\frac{\rho\Omega^2 R\psi_R}{|\nabla\psi|^4}\frac{R^4}{\mathscr{J}^2}\hat{X}\hat{X}^*\right\}. \tag{A25}$$

The term tagged 9 is written as

$$\int d^3x\,[-\boldsymbol{\xi}\cdot(\rho\mathbf{v}\cdot\nabla\mathbf{v})\,\nabla\cdot\boldsymbol{\xi}^*] = \int ds\,d\theta\,2s\psi_0\mathscr{J} \times\left\{\rho\frac{R^5R_\theta}{\mathscr{J}^2}\frac{\Omega^2}{4s^2\psi_0^2}(\hat{V}+\hat{Z})\left[\frac{2RR_{\mathbf{s}}}{R^2}X^* + \frac{2RR_\theta}{R^2}(\hat{V}^*+\hat{Z}^*) + \hat{X}_s^* + \hat{V}_\theta^* + \hat{Z}_\theta^* + \frac{J\mathscr{J}}{R^2}\hat{Z}_\phi^*\right]\right\}. \tag{A26}$$

The term tagged 10 is written as

$$\int d^3x\,[-\boldsymbol{\xi}^*\cdot(\rho\mathbf{v}\cdot\nabla\mathbf{v})\,\nabla\cdot\boldsymbol{\xi}] = \int ds\,d\theta\,2s\psi_0\mathscr{J} \times\left\{\rho\frac{R^5R_\theta}{\mathscr{J}^2}\frac{\Omega^2}{4s^2\psi_0^2}(\hat{V}^*+\hat{Z}^*)\left[\frac{2RR_{\mathbf{s}}}{R^2}\hat{X} + \frac{2RR_\theta}{R^2}(\hat{V}+\hat{Z}) + \hat{X}_s + \hat{V}_\theta + \hat{Z}_\theta + \frac{J\mathscr{J}}{R^2}\hat{Z}_\phi\right]\right\}. \tag{A27}$$

The term tagged 11 is written as

$$\begin{aligned}\int d^3x[-\rho|\mathbf{v}\cdot\nabla\boldsymbol{\xi}|^2] &= \int ds\,d\theta\,2s\psi_0\mathscr{J}\left\{-\rho\frac{\Omega^2R^4}{4s^2\psi_0^2|\nabla\psi|^2\mathscr{J}^2}\left|\frac{\psi_R J\mathscr{J}}{R}\hat{Z} - 2s\psi_0\hat{X}_\phi\right|^2\right.\\ &\quad -\rho\frac{\Omega^2R^2}{4s^2\psi_0^2}|-2s\psi_0\theta_z\hat{X}+\psi_z\hat{V}+\psi_z\hat{Z}+J\hat{Z}_\phi|^2\\ &\quad \left.-\rho\frac{\Omega^2R^2|\nabla\psi|^2}{4s^2\psi_0^2}\left|-\frac{RJR_\theta}{\mathscr{J}|\nabla\psi|^2}\hat{Z} - \frac{\nabla\psi\cdot\nabla\theta}{|\nabla\psi|^2}2s\psi_0\hat{X}_\phi + \hat{V}_\phi+\hat{Z}_\phi\right|^2\right\}.\end{aligned} \tag{A28}$$

The term tagged 12 is written as

$$\begin{aligned}\int d^3x[\boldsymbol{\xi}^*\cdot(\boldsymbol{\xi}\cdot\nabla)\,\nabla p] &= \int ds\,d\theta\,2s\psi_0\mathscr{J}\\ &\quad\times\left\{(2s\psi_0R^2\mathscr{J}^{-1}p_{\psi\psi}\hat{X}+R^2\mathscr{J}^{-1}p_{\psi\theta}\hat{V}+R^2\mathscr{J}^{-1}p_{\psi\theta}\hat{Z})\right.\\ &\quad\times\frac{R^2}{2s\psi_0\mathscr{J}}\hat{X}^* + (2s\psi_0R^2\mathscr{J}^{-1}p_{\theta\psi}\hat{X}+R^2\mathscr{J}^{-1}p_{\theta\theta}\hat{V}\\ &\quad + R^2\mathscr{J}^{-1}p_{\theta\theta}\hat{Z})\frac{R^2\mathscr{J}^{-1}}{4s^2\psi_0^2}(\hat{V}^*+\hat{Z}^*) + \frac{p_\psi}{4s^2\psi_0^2}\\ &\quad\times\left\{(2s\psi_0R^2\mathscr{J}^{-1}\psi_{R\psi}\hat{X}+R^2\mathscr{J}^{-1}\psi_{R\theta}\hat{V}+R^2\mathscr{J}^{-1}\psi_{R\theta}\hat{Z})\right.\\ &\quad\times(R^2\mathscr{J}^{-1}R_s\hat{X}^*+R^2\mathscr{J}^{-1}R_\theta\hat{V}^*+R^2\mathscr{J}^{-1}R_\theta\hat{Z}^*)\\ &\quad+(2s\psi_0R^2\mathscr{J}^{-1}\psi_{z\psi}\hat{X}+R^2\mathscr{J}^{-1}\psi_{z\theta}\hat{V}+R^2\mathscr{J}^{-1}\psi_{z\theta}\hat{Z})\\ &\quad\times(R^2\mathscr{J}^{-1}Z_s\hat{X}^*+R^2\mathscr{J}^{-1}Z_\theta\hat{V}^*+R^2\mathscr{J}^{-1}Z_\theta\hat{Z}^*)\\ &\quad\left.+J^2\psi_RR\hat{Z}\hat{Z}^*\right\}\\ &\quad+\frac{p_\theta}{4s^2\psi_0^2}\left\{(2s\psi_0R^2\mathscr{J}^{-1}\theta_{R\psi}\hat{X}+R^2\mathscr{J}^{-1}\theta_{R\theta}\hat{V}+R^2\mathscr{J}^{-1}\theta_{R\theta}\hat{Z})\right.\\ &\quad\times(R^2\mathscr{J}^{-1}R_s\hat{X}^*+R^2\mathscr{J}^{-1}R_\theta\hat{V}^*+R^2\mathscr{J}^{-1}R_\theta\hat{Z}^*)\\ &\quad+(2s\psi_0R^2\mathscr{J}^{-1}\theta_{z\psi}\hat{X}+R^2\mathscr{J}^{-1}\theta_{z\theta}\hat{V}+R^2\mathscr{J}^{-1}\theta_{z\theta}\hat{Z})\\ &\quad\times(R^2\mathscr{J}^{-1}Z_s\hat{X}^*+R^2\mathscr{J}^{-1}Z_\theta\hat{V}^*+R^2\mathscr{J}^{-1}Z_\theta\hat{Z}^*)\\ &\quad\left.\left.+J^2\theta_zR\hat{Z}\hat{Z}^*\right\}\right\}.\end{aligned} \tag{A29}$$

The term tagged 13 is written as

$$\begin{aligned}\int d^3x\left[-\boldsymbol{\xi}^*\cdot\nabla\psi\,\boldsymbol{\xi}\cdot\nabla\left(\frac{\nabla\psi\cdot\mathbf{J}\times\mathbf{B}}{|\nabla\psi|^2}\right)\right] &= \int ds\,d\theta\,2s\psi_0\mathscr{J}\\ &\quad\times\left\{-\frac{R^2}{2s\psi_0\mathscr{J}}\hat{X}^*\,[2s\psi_0R^2\mathscr{J}^{-1}p_{\psi\psi}\hat{X}+R^2\mathscr{J}^{-1}p_{\psi\theta}\hat{V}\right.\\ &\quad+r^2\mathscr{J}^{-1}p_{\psi\theta}\hat{Z}]\\ &\quad+[2s\psi_0R^2\mathscr{J}^{-1}p_{\psi\theta}\hat{X}+R^2\mathscr{J}^{-1}p_{\theta\theta}\hat{V}+R^2\mathscr{J}^{-1}p_{\theta\theta}\hat{Z})\\ &\quad\times\frac{\nabla\psi\cdot\nabla\theta}{|\nabla\psi|^2}+p_\theta[2s\psi_0R^2\mathscr{J}^{-1}(\nabla\psi\cdot\nabla\theta/|\nabla\psi|^2)_\psi\hat{X}\\ &\quad+R^2\mathscr{J}^{-1}(\nabla\psi\cdot\nabla\theta/|\nabla\psi|^2)_\theta\hat{V}+R^2\mathscr{J}^{-1}(\nabla\psi\cdot\nabla\theta/|\nabla\psi|^2)_\theta\hat{Z}]\\ &\quad-[2s\psi_0R^2\mathscr{J}^{-1}(\rho\Omega^2R\psi_R/|\nabla\psi|^2)\psi\hat{X}\\ &\quad+R^2\mathscr{J}^{-1}(\rho\Omega^2R\psi_R/|\nabla\psi|^2)_\theta\hat{V}\\ &\quad\left.+R^2\mathscr{J}^{-1}(\rho\Omega^2R\psi_R/|\nabla\psi|^2)_\theta\hat{Z}]\right\}.\end{aligned} \tag{A30}$$

The term tagged 14 is written as

$$\int d^3x \left[-\boldsymbol{\xi}\cdot\nabla\psi\,\boldsymbol{\xi}^*\cdot\nabla\left(\frac{\nabla\psi\cdot\mathbf{J}\times\mathbf{B}}{|\nabla\psi|^2}\right)\right] = \int ds\, d\theta\, 2s\psi_0\mathscr{J}$$
$$\times\left\{-\frac{R^2}{2s\psi_0\mathscr{J}}\hat{X}\,[2s\psi_0R^2\mathscr{J}^{-1}p_{\psi\psi}\hat{X}^* + R^2\mathscr{J}^{-1}p_{\psi\theta}\hat{V}^* + R^2\mathscr{J}^{-1}p_{\psi\theta}\hat{Z}^*]\right.$$
$$+\,[2s\psi_0R^2\mathscr{J}^{-1}p_{\psi\theta}\hat{X}^* + R^2\mathscr{J}^{-1}p_{\theta\theta}\hat{V}^* + R^2\mathscr{J}^{-1}p_{\theta\theta}\hat{Z}^*)$$
$$\times\frac{\nabla\psi\cdot\nabla\theta}{|\nabla\psi|^2} + p_\theta[2s\psi_0R^2\mathscr{J}^{-1}(\nabla\psi\cdot\nabla\theta/|\nabla\psi|^2)_\psi\hat{X}^*$$
$$+\,R^2\mathscr{J}^{-1}(\nabla\psi\cdot\nabla\theta/|\nabla\psi|^2)_\theta\hat{V}^* \qquad \text{(A31)}$$
$$+\,R^2\mathscr{J}^{-1}(\nabla\psi\cdot\nabla\theta/|\nabla\psi|^2)_\theta\hat{Z}^*]$$
$$-\,[2s\psi_0R^2\mathscr{J}^{-1}(\rho\Omega^2R\psi_R/|\nabla\psi|^2)\psi\hat{X}^*$$
$$+\,R^2\mathscr{J}^{-1}(\rho\Omega^2R\psi_R/|\nabla\psi|^2)_\theta\hat{V}^*$$
$$\left.+\,R^2\mathscr{J}^{-1}(\rho\Omega^2R\psi_R/|\nabla\psi|^2)_\theta\hat{Z}^*]\right\}.$$

The term tagged 15 is written as

$$\int d^3x \left\{-\boldsymbol{\xi}^*\cdot(\boldsymbol{\xi}\cdot\nabla)\,\nabla\psi\frac{\nabla\psi\cdot\mathbf{J}\times\mathbf{B}}{|\nabla\psi|^2}\right\} = \int ds\, d\theta\, 2s\psi_0\mathscr{J}$$
$$\times\left\{-\frac{1}{4s^2\psi_0^2}\{(2s\psi_0R^2\mathscr{J}^{-1}\psi_{R\psi}\hat{X} + R^2\mathscr{J}^{-1}\psi_{R\theta}\hat{V}\right.$$
$$+\,R^2\mathscr{J}^{-1}\psi_{R\theta}\hat{Z})$$
$$\times(R^2\mathscr{J}^{-1}R_s\hat{X}^* + R^2\mathscr{J}^{-1}R_\theta\hat{V}^* + R^2\mathscr{J}^{-1}R_\theta\hat{Z}^*)$$
$$+\,(2s\psi_0R^2\mathscr{J}^{-1}\psi_{z\psi}\hat{X} + R^2\mathscr{J}^{-1}\psi_{z\theta}\hat{V} + R^2\mathscr{J}^{-1}\psi_{z\theta}\hat{Z}) \qquad \text{(A32)}$$
$$\times(R^2\mathscr{J}^{-1}Z_s\hat{X}^* + R^2\mathscr{J}^{-1}Z_\theta\hat{V}^* + R^2\mathscr{J}^{-1}Z_\theta\hat{Z}^*)$$
$$\left.+\,J^2\psi_RR\hat{Z}\hat{Z}^*\}\left\{p_\psi + \frac{\nabla\psi\cdot\nabla\theta}{|\nabla\psi|^2}p_\theta - \frac{\rho\Omega^2R\psi_R}{|\nabla\psi|^2}\right\}\right\}.$$

The term tagged 16 is written as

$$\int d^3x \left\{\frac{|\boldsymbol{\xi}\cdot\nabla\psi|^2}{|\nabla\psi|^2}\nabla\psi\cdot\nabla\left(\frac{\nabla\psi\cdot\mathbf{J}\times\mathbf{B}}{|\nabla\psi|^2}\right)\right\}$$
$$= \int ds\, d\theta\, 2s\psi_0\mathscr{J}\left\{\frac{R^4}{\mathscr{J}^2|\nabla\psi|^2}\hat{X}\hat{X}^*[p_{\psi\psi}|\nabla\psi|^2 + p_{\psi\theta}\nabla\psi\cdot\nabla\theta\right.$$
$$+\,(p_{\theta\psi}|\nabla\psi|^2 + p_{\theta\theta}\nabla\psi\cdot\nabla\theta)\frac{\nabla\psi\cdot\nabla\theta}{|\nabla\psi|^2}$$
$$+\,p_\theta\frac{(\nabla\psi\cdot\nabla\theta)_\psi|\nabla\psi|^2 + (\nabla\psi\cdot\nabla\theta)_\theta\nabla\psi\cdot\nabla\theta}{|\nabla\psi|^2} \qquad \text{(A33)}$$
$$-\,p_\theta\frac{\nabla\psi\cdot\nabla\theta}{|\nabla\psi|^4}(|\nabla\psi|^2_\psi|\nabla\psi|^2 + |\nabla\psi|^2_\theta\nabla\psi\cdot\nabla\theta)$$
$$-\,(\rho\Omega^2R\psi_R/|\nabla\psi|^2)_\psi|\nabla\psi|^2$$
$$\left.-\,(\rho\Omega^2R\psi_R/|\nabla\psi|^2)_\theta\nabla\psi\cdot\nabla\theta\right\}.$$

APPENDIX B: A TOROIDALLY ROTATING EQUILIBRIUM MODEL

A simple equilibrium model has been developed to provide input to the instability analysis discussed in this paper. For theories and computational schemes for plasma equilibria Refs. [45–49] and references cited in them should be consulted. In the model used for instability analysis, we assume constant toroidal differential rotation Ω and constant density ρ on each flux surface. Hence $\Omega = \Omega(\psi)$ and $\rho = \rho(\psi)$. The plasma pressure $p(R, Z)$ can be now given by means of another flux function $\Pi(\psi)$; i.e., $p(R, Z) = \Pi(\psi) + \frac{1}{2}\rho\Omega^2R^2$. The toroidal flux function RB_ϕ can also be a function of the poloidal flux; i.e., $RB_\phi = F(\psi)$. These assumptions help us extend the static plasma equilibrium calculations easily into toroidally rotating regime compared to more involved schemes in Refs. [48–49]. It should be noted that we do not explicitly assume isothermal or isentropic flux surfaces. The model chosen here is based on computational simplicity as illustrated in the following.

The $\Pi(\psi)$ and $F^2(\psi)$ are parametrized polynomially as

$$\Pi(\psi) = \sum_1^n p_i(\psi/\psi_0)^{i+1}, \qquad \text{(B1)}$$

$$F^2(\psi) = \sum_1^n t_i(\psi/\psi_0)^{i+1}. \qquad \text{(B2)}$$

The equilibrium equation can be conveniently solved by an iterative procedure, and, finally, all the variables can be scaled to their actual values to provide a prescribed toroidal current. The flux equation for the normalized flux variable Ξ is given by

$$\Delta^*\Xi = -\frac{\mu_0p_1}{\psi_0^2}\left[\frac{1}{2R^2}\frac{\partial\overline{F}^2}{\partial\Xi} + \frac{\partial\overline{\Pi}}{\partial\Xi} + \frac{1}{2}R^2\frac{\partial}{\partial\Xi}(\overline{\rho}\Omega^2)\right]$$
$$= -\lambda\left[\frac{1}{2R^2}\frac{\partial\overline{F}^2}{\partial\Xi} + \frac{\partial\overline{\Pi}}{\partial\Xi} + \frac{1}{2}R^2\frac{\partial}{\partial\Xi}(\overline{\rho}\Omega^2)\right], \qquad \text{(B3)}$$

wherein new functions $\overline{F} = F/p_1$, $\overline{\Pi} = \Pi/p_1$ and $\overline{\rho} = \rho/p_1$, and $\Xi = \psi/\psi_0$ are introduced. By specifying the plasma boundary and the total toroidal current I, the equilibrium can be solved. As the iterations progress, the value of λ is refined. Once the magnetic axis is located by solving the equation in the generalized polar coordinates while keep-

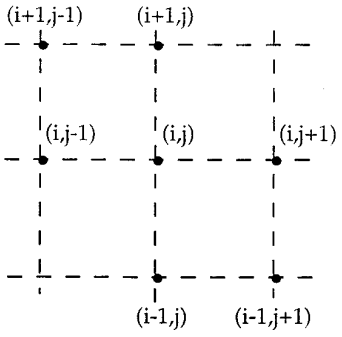

FIG. B1. Seven-point stencil used in the multigrid equilibrium solution.

ing the origin at R_0, subsequent sets of iterations can be done by anchoring the origin at new magnetic axis positions. The flux functions are specified by introducing nonzero coefficients for p_0/p_1, t_1/p_1, etc. Computationally the solution is implemented as follows. The elliptic operator in (B3) is transformed to generalized polar coordinates (a, θ) as

$$\frac{|\nabla a|^2}{R^2}\frac{\partial^2 \Xi}{\partial a^2} + 2\frac{\nabla a\cdot\nabla\theta}{R^2}\frac{\partial^2\Xi}{\partial a\,\partial\theta} + \frac{|\nabla\theta|^2}{R^2}\frac{\partial^2\Xi}{\partial\theta^2} + \frac{1}{\mathscr{J}}\frac{\partial}{\partial a}\left(\mathscr{J}\,\frac{|\nabla a|^2}{R^2}\right)\frac{\partial\Xi}{\partial a} + \frac{1}{\mathscr{J}}\frac{\partial}{\partial a}\left(\mathscr{J}\,\frac{\nabla a\cdot\nabla\theta}{R^2}\right)\frac{\partial\Xi}{\partial\theta} + \frac{1}{\mathscr{J}}\frac{\partial}{\partial\theta}\left(\mathscr{J}\,\frac{\nabla a\cdot\nabla\theta}{R^2}\right)\frac{\partial\Xi}{\partial a} + \frac{1}{\mathscr{J}}\frac{\partial}{\partial\theta}\left(\mathscr{J}\,\frac{|\nabla\theta|^2}{R^2}\right)\frac{\partial\Xi}{\partial\theta} = \mathscr{S}, \tag{B4}$$

where $\mathscr{S}$ is an appropriate source term. The cross derivative is discretized on a seven-point stencil:

$$\frac{\partial^2\Xi}{\partial a\,\partial\theta} = \frac{(\Xi_{i+1,j} + \Xi_{i-1,j} + \Xi_{i,j+1} + \Xi_{i,j-1} - 2\Xi_{ij} - \Xi_{i+1,j-1} - \Xi_{i-1,j+1})}{2\,\Delta a\,\Delta\theta}. \tag{B5}$$

This seven-point stencil is illustrated in Fig. B1. By specifying toroidal current and profile factors and other plasma parameters, Eq. (B4) is iteratively solved by a multigrid scheme.

REFERENCES

1. I. B. Bernstein, E. A. Frieman, M. D. Kruskal, and R. M. Kulsrud, *Proc. R. Soc. London Sect. A* **244,** 17 (1958).
2. K. Brau, M. Bitter, R. J. Goldston, D. Manos, K. McGuire, and S. Suckewer, *Nucl. Fusion* **23,** 1643 (1983).
3. A. Bondeson, R. Iacono, and A. Bhattacharjee, *Phys. Fluids* **30,** 2167 (1987).
4. H. Grad, "GCP Model," in *Proceedings, Symp. Electromag. Fluid Dynamics of Gas, Plasmas, Polytech. Inst. of Brooklyn, 1961,* p. 37.
5. A. Bondeson and R. Iacono, *Phys. Fluids* **B1,** 1431 (1989).
6. S. R. Choudhury and R. V. E. Lovelace, *Astrophys. J.* **302,** 188 (1986).
7. A. Miura and P. L. Pritchett, *J. Geophys. Res.* **87,** 7431 (1982).
8. T. P. Ray and A. I. Ershkovich, *Mon. Not. R. Astron. Soc.* **204,** 821 (1983).
9. A. Ferrari, E. Trussoni, and L. Zaninetti, *Mon. Not R. Astron. Soc.* **196,** 1051 (1981).
10. E. Hameiri, *Phys. Fluids* **26,** 1643 (1983).
11. J. A. Tataronis and M. Mond, *Phys. Fluids* **30,** 84 (1987).
12. P. Pietrini and G. Torricelli-Ciamponi, *Phys. Fluids B* **1,** 923 (1989).
13. E. Corbelli and G. Torricelli-Ciamponi, *Phys. Fluids B* **2,** 828 (1990).
14. A. Ferrari, in *Unstable Current Systems and Plasma Instabilities in Astrophysics, IAU Symposium,* Vol. 107, edited by M. R. Kundu and G. D. Holman (Reidel, Dordrecht, 1985), p. 393.
15. D. A. Clarke, M. L. Norman, and J. O. Burns, *Astrophys. J.* **311,** L63 (1986).
16. H. Cohn, *Astrophys. J.* **269,** 500 (1983).
17. R. Fiedler and T. W. Jones, *Astrophys. J.* **283,** 532 (1984).
18. E. Frieman and M. Rotenberg, *Rev. Mod. Phys.* **32,** 898 (1960).
19. S. Chandrasekhar, *Ellipsoidal Figures of Equilibrium,* (Yale Univ. Press, New Haven, CT, 1969).
20. J. L. Tassoul, *The Theory of Rotating Stars* (Princeton Univ. Press, Princeton, NJ, 1979).
21. J. Pedlosky, *Geophysical Fluid Dynamics* (Springer-Verlag, New York, 1979).
22. E. Hameiri, *J. Math. Phys.* **22,** 2080 (1981).
23. J. A. Almaguer, E. Hameiri, J. Herrera, and D. D. Holm, *Phys. Fluids* **31,** 1930 (1988).
24. D. Lynden-Bell and J. P. Ostriker, *Mon. Not. R. Astron. Soc.* **136,** 293 (1967).
25. J. M. Bardeen, J. L. Freidman, B. F. Schutz, and R. Sorkin, *Astrophys. J.* **217,** L49 (1977).
26. J. L. Freidman and B. F. Schutz, *Astrophys. J.* **221,** 937 (1978).
27. B. F. Schutz, *Astrophys. J.* **232,** 874 (1979).
28. N. R. Lebovitz, *Geophys. Astrophys. Fluid Dynamics* **46,** 221 (1989).
29. N. G. Van Kampen and B. U. Felderhof, *Theoretical Methods in Plasma Physics* (North Holland, New York, 1967).
30. R. Gruber, F. Troyan, D. Berger, L. C. Bernard, S. Rousset, R. Schreiber, W. Kerner, W. Schneider, and K. V. Roberts, *Comput. Phys. Commun.* **21,** 323 (1981).
31. R. Gruber and J. Rappaz, *Finite Element Methods in Linear Ideal Magnetohydrodynamics* (Springer-Verlag, Berlin, 1985).
32. X. H. Wang and A. Bhattacharjee, *Phys. Fluids B* **2,** 2346 (1990).
33. F. Waelbrock and L. Chen, *Phys. Fluids B* **3,** 601 (1991).
34. V. Varadarajan, Ph.D. thesis, University of Illinois at Urbana-Champaign, 1993.
35. R. C. Grimm, J. M. Greene, and J. L. Johnson, *Methods Comput. Phys.* **16,** 253 (1976).
36. W. Kerner, *Nucl. Fusion* **16,** 643 (1976).
37. S. G. Mikhlin, *The Problem of the Minimum of a Quadratic Functional* (Holden-Day, San Francisco, 1965), Sections 11–13.
38. C. Canuto, M. Y. Hussaini, A. Quarteroni, and T. A. Zang, *Spectral*

Methods in Fluid Dynamics (Springer-Verlag, New York/Berlin, (1988).

39. G. Strang and G. G. Fix, *Analysis of the Finite Element Method* (Prentice–Hall, Englewood Cliffs, NJ, 1973).
40. T. Takeda, Y. Shimomura, M. Ohta, and M. Yoshikawa, *Phys. Fluids* **15**(12), 2193 (1972).
41. J. H. Wilkinson and C. Reinsch, *Linear Algebra* (Springer-Verlag, Berlin, 1971).
42. V. D. Shafranov, *Soviet Phys. Tech. Phys.* **15,** 175 (1970).
43. M. S. Chance, J. M. Greene, R. C. Grimm, J. L. Johnson, J. Manickam, W. Kerner, D. Berger, L. C. Bernard, R. Gruber, and F. Troyon, *J. Comput. Phys.* **28,** 1 (1978).
44. M. F. F. Nave, D. J. Campbell, E. Joffrin, F. B. Marcus, G. Sadler, P. Smeulders, and K. Thomsen, *Nucl. Fusion* **31,** 697 (1991).
45. H. P. Zehrfeld and B. J. Green, *Nucl. Fusion.* **12,** 569 (1972).
46. H. Strauss, *Phys. Fluids* **16,** 1377 (1973).
47. E. K. Maschke and H. Perrin, *Plasma Phys.* **22,** 579 (1980).
48. W. Kerner and O. Jandl, *Comput. Phys. Commun.* **31,** 269 (1984).
49. W. A. Cooper and S. P. Hirshman, *Plasma Phys. Controlled Fusion* **29,** 933 (1987).